Multiphase magmatic flows at Yucca Mountain, Nevada

S. Dartevelle[1] and G. A. Valentine[2]

[1]   The proposed Yucca Mountain radioactive waste repository is sited in southern Nevada in a region that has experienced sporadic basaltic volcanism since the late Miocene. Volcanic risk assessment for the proposed repository requires estimating the consequences of a new monogenetic volcano intersecting the underground facility during its 10^4–10^6 year performance period. We report numerical studies aimed at understanding the range of processes and dynamic parameter values that could accompany intersection of an open repository drift by a volatile-rich trachybasaltic magma as it ascends in a dike. We focus on one end-member type of magmatic behavior, namely, a fragmented magmatic mixture under pressure interacting with an underground cavity. Initial and boundary conditions are based upon field data and previous modeling studies of the interaction between vertically propagating dikes and a repository opening. The calculations are two-dimensional and time-dependent and are conducted with the multiphase hydrodynamics code GMFIX. Calculations indicate that gas-particle mixtures, as they rise from below and interact with horizontal openings, form complex flow patterns involving varying degrees of recirculation and deposition of pyroclasts. Dynamic pressures are up to 10^6 Pa but are more typically on the order of 10^3 to 10^4 Pa. The geometry and number of outlets play a key role in determining the types of flow patterns, as do volatile contents and the degree of fragmentation. The detailed numerical simulations provide information that will be used to confirm the adequacy of simplified probabilistic consequence models used in risk assessments.

1.   Introduction

[2]   Yucca Mountain, Nevada, is the proposed site for the United States' first permanent geologic repository for high-level radioactive waste (predominantly from civilian power reactors). The site is within a region that has experienced sporadic basaltic volcanism since the late Miocene [*Vaniman et al.*, 1982; *Crowe et al.*, 1982; *Crowe*, 1986; *Fleck et al.*, 1996; *Valentine and Perry*, 2006, 2007], necessitating the assessment of risk from a potential new basaltic volcano intersecting the repository at some time during its performance period (10^4–10^6 years). Although the probability of such an event is relatively low, the consequences are potentially large. Event probability has been addressed by a formal expert elicitation process that assessed extensive geologic, geochemical, geophysical, and geochronological data as well as modeling [*Bechtel SAIC Company* (*BSC*), 2004a], building on approaches such as those of *Crowe et al.* [1982], *Connor and Hill* [1995], and *Connor et al.* [2000]. Potential consequences of such an event are constrained by

characterization of the physical processes associated with formation of monogenetic basaltic volcanoes in the region, using a range of field observations [*Valentine et al.*, 2005, 2006, 2007; *Valentine and Krogh*, 2006; *Valentine and Keating*, 2007; *Keating et al.*, 2008], as well as by theoretical modeling of scenarios that could result from intersection of the plumbing of such a volcano with the repository [*BSC*, 2004b].

[3]   The focus of this paper is on one aspect of the consequences analysis, namely, the phenomena that would be associated with flow of rising gas-pyroclast mixtures into subsurface repository openings (drifts) [*Woods et al.*, 2002; *Dartevelle and Valentine*, 2005, 2007b]. Large uncertainties in many key parameters such as magma volatile contents and specific subsurface geometries of intersection of the repository by volcanic plumbing, as well as the complex three-dimensional nature of a particular event, complicate detailed predictions of individual magma-repository scenarios. Therefore, our goal is to understand the basic processes and ranges of parameter values for generalized magma-repository interactions. We consider the flow of gas-pyroclast mixtures to be one end-member of magma-repository interaction; the other end-member involves ascending gas-poor magma (unfragmented), which has been treated elsewhere and will be summarized briefly in this paper. We use the numerical code GMFIX version 1.62 as the computational tool to explore the inherently multiphase

[1]Earth and Environmental Sciences Division, Los Alamos National Laboratory, Los Alamos, New Mexico, USA.
[2]Department of Geology, State University of New York at Buffalo, Buffalo, New York, USA.
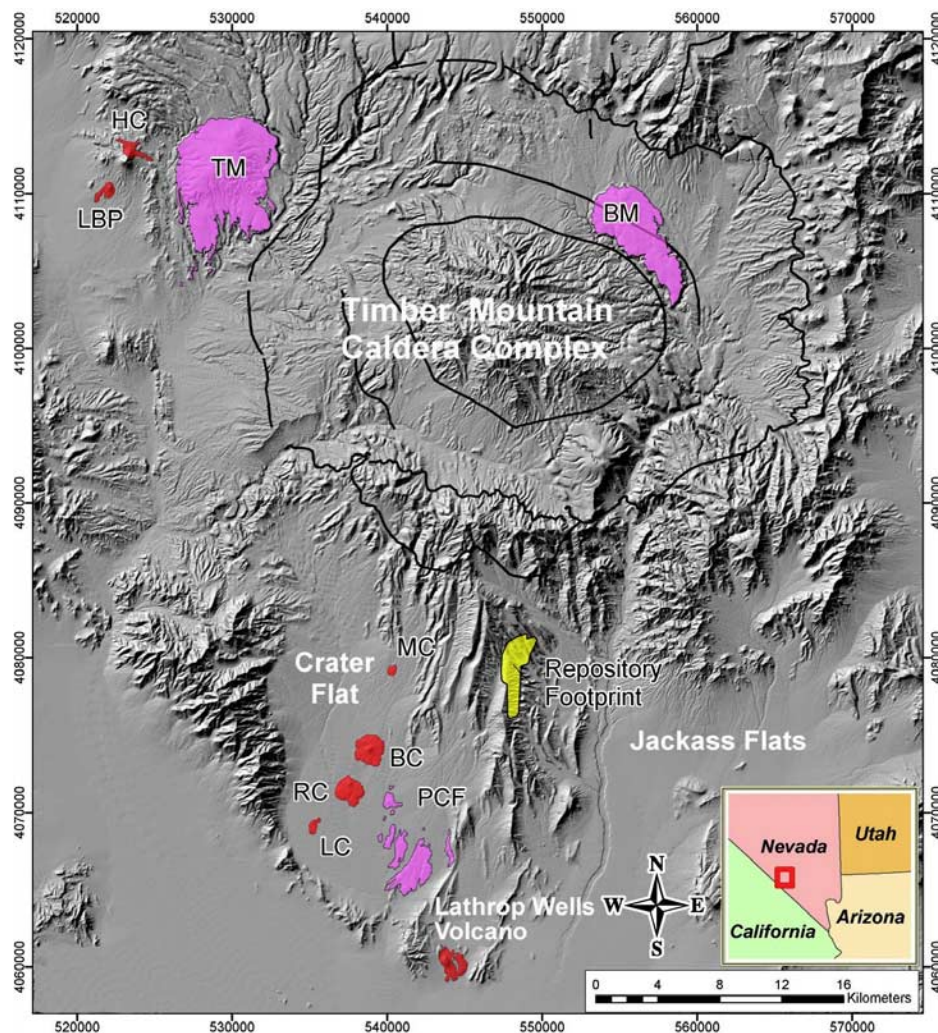
Figure 1. Digital elevation model of the Yucca Mountain area showing distribution of Plio-Pleistocene basaltic volcanoes, caldera outlines from mid-Miocene activity [*Wahl et al.*, 1997], and major basins (Crater Flat, Jackass Flats). Pliocene volcanoes are Thirsty Mountain (TM), Buckboard Mesa (BM), and Pliocene Crater Flat (PCF). Pleistocene volcanoes in Crater Flat (LC, Little Cones; RC, Red Cone; BC, Black Cone; MC, Makani Cone) are ~1 Ma [*Fleck et al.*, 1996; *Perry et al.*, 1998; *Valentine et al.*, 2006]. Little Black Peak (LBP) and Hidden Cone (HC) are ~0.32 and 0.37 Ma, respectively [*Fleck et al.*, 1996]. Lathrop Wells volcano is ~80 ka [*Heizler et al.*, 1999]. Modified from *Valentine et al.* [2007].

dynamics, following *Dartevelle and Valentine* [2005]. This paper begins with a summary of recent (Quaternary) volcanism in the region as well as data pertaining to subsurface plumbing of those volcanoes and the repository design. We review previous studies of the interaction between rising basaltic magmas and the proposed repository at depths of ~250–350 m. The field data and repository design provide a basis for developing problem geometry and initial/boundary conditions for multiphase flow simulations. We briefly describe the computational approach and how it is validated for the specific application at hand. We then present results of simulations that elucidate the range of dynamics and parameter values that could occur within the repository in the event that it is intersected by a rising gas-pyroclast mixture. The paper closes with a discussion of the limitations of the model results as well as how the general approach can be taken into other types of volcanic risk studies.

2. Volcanological Context and Repository Design

[4] Volcanoes that erupted in the Southwest Nevada Volcanic Field during the Quaternary provide the principal analogs for a potential future event at Yucca Mountain. Quaternary activity resulted in the formation of eight small volume (between 0.002 km^3 and 0.12 km^3) volcanoes (Figure 1), each consisting of one or two lava flow fields (typically ~1 km long) and a scoria cone [*Valentine and Perry*, 2006]. Composition of the volcanoes is mainly trachybasaltic (or hawaiitic) [*Vaniman et al.*, 1982; *Bradshaw and Smith*, 1994; *Fleck et al.*, 1996; *Perry et al.*, 1998; *Valentine and Perry*, 2007]; the rare presence of amphibole as well as experimental and fluid inclusion data indicate that

volatile contents were likely relatively high (1.2–4.6 wt % H_2O [*Nicholis and Rutherford*, 2004]). Each volcano is inferred on the basis of facies characteristics to have erupted over a period of several months to a few years [*Valentine et al.*, 2006, 2007] with a range of eruptive styles. These styles include (1) Strombolian activity characterized by temporally discrete, low fountains or bursts of coarse ejecta; (2) violent Strombolian activity characterized by sustained buoyant eruption columns of ash and lapilli up to several kilometers high; and (3) effusive lavas. The volcanoes do not record a characteristic sequence of styles. Rather, some volcanoes apparently had early cone building phases of potentially violent Strombolian activity followed by less energetic Strombolian eruptions (e.g., Red Cone and Black Cone volcanoes [*Valentine et al.*, 2006]), while others had the opposite cone-building sequence (e.g., Lathrop Wells, Hidden Cone, and Little Black Peak volcanoes [*Valentine et al.*, 2007; *Valentine and Keating*, 2007]). Lavas appear to have effused primarily from the bases of the growing cones at a range of times during formation of each volcano, including contemporaneously with pyroclastic cone-building activity [*Valentine et al.*, 2006, 2007]. Most of the lavas are inferred to have been fed by lateral breakouts from the main feeding conduits, near the interface between the cone and the preexisting ground surface.

[5] Our interest in this paper is in the subsurface processes that might occur at repository depth, therefore it is important to understand the shallow plumbing of these small monogenetic, trachybasaltic volcanoes. Field evidence from eroded basaltic volcanoes in the region shows that they are fed by dikes that locally flare in the uppermost ~100 m (mainly in the upper 50 m) to form conduits that feed scoria and spatter cones [*Keating et al.*, 2008]. On the basis of field observations [*Valentine and Krogh*, 2006; *Valentine and Perry*, 2006; *Keating et al.*, 2008], dikes are inferred to have widths ranging mainly between 1 and 12 m (mean of 8 m), and lengths of ~0.4–8 km (mean of 2 km) at repository depths [*Sandia National Laboratories* (*SNL*), 2007a]. Feeder dikes for basaltic volcanoes that we have studied in the region nearly ubiquitously occupy preexisting normal faults, even though the common ~N–S strikes of those faults reflect older principal stress orientations that were oblique to the late Miocene-Quaternary principle stresses, which would have dikes striking ~N30°E if they had been unaffected by earlier structures [*Valentine and Krogh*, 2006; *Perry et al.*, 2006; *Valentine and Keating*, 2007; *Keating et al.*, 2008]. Volcanoes that are sufficiently eroded to expose feeder dikes commonly also have up to four additional parallel dikes that seem to be subsidiary, but coeval, to the main feeder dike and that did not vent at the surface (even though in at least two cases the tips of these subsidiary dikes only stopped propagating within several tens of meters of the surface [*Valentine and Krogh*, 2006; *Keating et al.*, 2008]). Basaltic magma at one volcanic center formed a small sill complex at depths of ~150–250 m, but this appears to be related to a rather unique structural setting (Paiute Ridge [*Valentine and Krogh*, 2006]), whereas only one other volcano that we have studied had a sill that extended laterally up to 30 m from the feeder dike at a paleodepth also of ~30 m (Basalt Ridge [*Keating et al.*, 2008]). We consider the most important

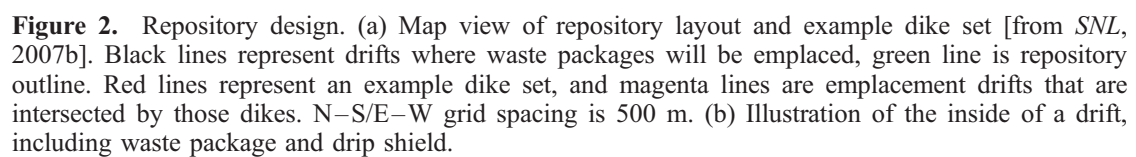intrusion type for our analyses at repository depth to be that of a dike.

[6] These geologic data must be combined with information about the design of the proposed repository in order to set up appropriate models of magma-repository interaction. The repository design extends in the subsurface over an area of slightly more than 5 km in the N–S direction and ~2 km in the E–W direction (Figure 2a). Cylindrical waste packages (~2 m in diameter and ~6 m long) will be emplaced in open, E–NE trending drifts that are several hundred meters long (variable over the repository footprint), with cross-section diameters of 5.5 m (Figure 2b). In the current design, drip shields will be placed over the waste packages in order to minimize contact between the packages and waters that might seep downward through the thick sequence of unsaturated rocks as well as any rockfall that might occur in a drift. Horizontal spacing between drifts will be ~80 m, composed of intact country rock. As shown by the example in Figure 2a, the most likely orientations of potential basaltic dikes are at high angles to the drift orientation, and for purposes of the modeling described here the intersection is treated as perpendicular.

3. Previous Studies

[7] Previous work on the interaction between basaltic magma and horizontal openings has been of three types: (1) studies of the effects of repository openings on the coupled solid-fluid mechanics of dike propagation [*BSC*, 2004b]; (2) simplified theoretical and laboratory models of flow of magma from a vertical dike into an open drift, including incompressible (lava [*BSC*, 2004b]) and explosive (pyroclastic [*Woods et al.*, 2002]) flow and longer-term mass exchange between vertical and horizontal fluid pathways [*Menand and Phillips*, 2007]; and (3) two-dimensional, time-dependent multiphase modeling of flow into and out of drifts [*Dartevelle and Valentine*, 2005]. We briefly review the results of these previous studies, focusing on aspects that are pertinent to the subject of this paper.

3.1. Dike Propagation

[8] *BSC* [2004b] reports modeling results aimed at understanding the potential impacts of repository openings on vertical dike propagation both at the scale of an entire dike and at the more detailed scale of a propagating dike tip interacting with a single drift. A propagating dike has a leading crack, followed by a void region referred to as the tip cavity, and finally by magma behind a magma front [e.g., *Rubin*, 1995]. Calculations of *BSC* [2004b] indicate that the leading crack of an upward propagating dike will rapidly accelerate ahead of the magma front as the dike tip nears the Earth's free surface, resulting in a growing tip cavity region (note that in these analyses the magma is assumed to be incompressible fluid, therefore not accounting for the presence of bubbles or a situation of fragmented flow). As a result of this effect, the tip of a dike propagating upward through Yucca Mountain will advance rapidly through the repository horizon and likely reach, or be near to, the surface before the magma front reaches the repository. Near drifts, the rising magma front may experience a delay in its upward flow on the order of tens of minutes as magma flows into intersected drifts, but is ultimately most likely to

A.

B.

Carbon Steel Sets
(no barrier to flow)

Basket Materials
(Carbon Steel/Aluminum)

Waste Form
(Spent Fuel, Glass)

Drip Shield
(Titanium)

Waste Package
(Alloy 22/Stainless Steel)

Emplacement Pallet
(Alloy 22/Stainless Steel)

Invert Beam
(Carbon Steel)

Invert Ballast
(Crushed Tuff Ballast)

00584DC_056.ai

Figure 2. Repository design. (a) Map view of repository layout and example dike set [from *SNL*, 2007b]. Black lines represent drifts where waste packages will be emplaced, green line is repository outline. Red lines represent an example dike set, and magenta lines are emplacement drifts that are intersected by those dikes. N–S/E–W grid spacing is 500 m. (b) Illustration of the inside of a drift, including waste package and drip shield.

continue its ascent toward the surface, following the existing pathway that was established by the crack tip. The fraction of strike length for a potential dike that would be intersected by initially open drifts (5.5 m diameter) versus intact rock between drifts (80 m) is relatively small, ~7%. Along most of the strike of such a dike, between drifts, the magma front would continue to rise (albeit at a rate that is reduced by the localized diversion of magma into drifts). This also indicates that vertical dike propagation would be relatively unaffected by the presence of repository openings. *BSC* [2004b] also presents more detailed modeling of the effects of local stress perturbations due to the repository (i.e., from the openings themselves or from the heat produced by radioactive decay during the initial ~2000 years after waste emplacement). Results indicate that stress changes due to the openings alone would have little effect on ultimate upward propagation of a dike along the same path it would take if the repository were absent, but stress changes due to heating would decrease the crack speed through the repository by about an order of magnitude, and increase magma overpressures (to ~6 MPa).

3.2. Simplified Theoretical Models and Laboratory Experiments of Magma Flow Into and Out of Drifts

[9] As discussed above, there are two end-member types of flow into (and out of) drifts: (1) flow of gas poor magma as an incompressible viscous fluid and (2) compressible flow of fragmented magma and a continuous gas phase (i.e., pyroclastic flow). Flow into drifts has been treated with simplified theoretical models for these two end-members [*Woods et al.*, 2002; *BSC*, 2004b]. Intermediate between these two are flows that are bubbly but where the continuous phase is incompressible basaltic melt. *Menand and Phillips* [2007] conducted experiments to study the role of a horizontal body on the mass transfer processes in a vertical conduit with bubbles.

[10] *BSC* [2004b] presents theoretical results for flow of incompressible, viscous magma from a vertical dike into a drift. The analysis combines analytical solutions for flow over a weir (i.e., flow through a semicircular hole in a vertical wall, similar to a situation where the magma front in the feeding dike does not rise completely to the top of a drift and magma "spills" into the drift), flow through a circular orifice (appropriate for a situation where the magma front in a dike rises above the top of a drift as the drift fills), and flow through a tube (i.e., when the magma completely fills a drift and forms a front that propagates down drift). The calculations use fluid viscosities of 10 and 40 Pa s, which are calculated liquidus viscosities for the trachybasaltic magmas typical of Quaternary activity in the region [*SNL*, 2007a], and are likely somewhat lower than might occur in a real situation where groundmass crystals and small bubbles might be present in the magma. In addition, the calculations do not consider heat transfer and temperature dependent viscosity, but filling processes in the drifts are considered to be sufficiently rapid to minimize heat loss through the surrounding rocks. The calculations suggest that incompressible viscous magma can fill a drift in time scales of tens to a few hundreds of seconds [*BSC*, 2004b] although this is likely an underestimate because the analysis did not include viscous drag in the dike.

[11] *Woods et al.* [2002] focused on the flow of a gas-particle mixture from a dike and through repository openings. They considered three scenarios. The first is a situation where the vertically ascending dike continues to the surface after it intersects the repository. In this situation they suggested that eruptive conduits would form preferentially over drifts. The second scenario considered by *Woods et al.* [2002] assumes that a gas-particle mixture flows down intersected drifts and then exits upward along secondary dikes that formed as a result of high local and transient pressures at the closed ends of dikes caused by reflection of shocks generated by rapid expansion of the mixture into the drifts. *BSC* [2004b] reports arguments as to why this mechanism for formation of secondary dikes is unlikely. In the analyses presented in section 7, we show the impacts of such secondary exits on multiphase flow in drifts; although we agree that these exits are unlikely to form, these results do not fully preclude the possibility. The final scenario considered by *Woods et al.* [2002] has the gas-particle mixture flowing through intersected drifts and eventually flooding the repository and erupting out vertical ventilation shafts. We consider this unlikely because, unlike the simplification used in the *Woods et al.* [2002] analysis, gas-particle mixtures do not remain homogeneously mixed but rather particles (pyroclasts) separate from the gas phase as a flow field evolves in the geometry of interest (*Woods et al.* [2002] assumed steady flow of a gas-particle mixture where the two phases are perfectly coupled in terms of heat and momentum, and used a one-dimensional approach to model the flows in their three scenarios). Also, repository design may include backfill of access tunnels connecting drifts to each other (or rockfall during the long lifetime of the repository might have a similar effect), thus forming a barrier to pyroclastic flow. Nevertheless, *Woods et al.* [2002] provide a useful starting point for addressing gas-particle flows associated with magma-drift interactions.

[12] Once a flow path has been established to the surface, it is important to consider the processes that might occur during the ensuing months to years that the monogenetic volcanic system might be active. Many basaltic volcanoes that experience Strombolian eruptive activity have phases during which a relatively stationary column of liquid magma exists in the volcanic conduit and plumbing. Bubbles form by exsolution of volatiles and these tend to rise and set up circulations in the shallow magma system (in fact, classical Strombolian explosions are caused by the bursting of large bubbles at the surface of such a magma column). Experiments by *Menand and Phillips* [2007] and *Menand et al.* [2008] demonstrate that if a horizontal pipe or sill is connected to the vertical feeding conduit of such a volcano, a flow pattern can be set up in which some bubbly magma is diverted into the horizontal body. As it flows horizontally away from the main conduit, bubbles continue to rise and form a foam at the top of the horizontal body, while the bottom of the body becomes enriched in denser, degassed magma. The interaction of the foam and degassed magma sets up an exchange flow between the vertical conduit (or dike) and the horizontal body. The impacts of this process in terms of potentially entraining waste from waste packages that are down drift from a dike-drift intersection have not been fully assessed, but there is an indication that periods of relatively low energy eruptive

Table 1. Numerical Properties for All Simulations

Geometry	Cartesian
Spatial discretization	MUSCL (second-order accurate)
Time discretization	first-order accurate
Linear equation solver	BI-CIGSTAB
Parallelization scheme	SMP/OPEN-MP
Outlet boundary	constant pressure and temperature outflow (PO)
Wall	no-slip wall (all phases)

activity might result in entrainment of some waste from down-drift packages. Similar return flow circulations are observed in some of the numerical results presented in section 7 of this paper and by *Dartevelle and Valentine* [2005], although they reflect different dynamics than those of *Menand and Phillips* [2007].

3.3. Multiphase Numerical Simulations

[13] *Dartevelle and Valentine* [2005] conducted an initial set of time-dependent, multiphase hydrodynamics numerical simulations aimed at understanding the interaction between a rising gas-particle mixture and an open drift. For the initial and boundary conditions they studied, it was shown that the gas-particle mixture enters a horizontal drift along the ceiling of the drift due to the upward momentum of the mixture at the dike-drift intersection. The mixture flows along the roof for some tens of meters before it begins to settle downward. If the mixture reaches the closed end of a drift before it settles to the floor it will turn and travel back toward the dike-drift intersection along the drift floor, setting up a transient return flow. *Dartevelle and Valentine* [2005] also modeled the decompression of an already filled drift, as might happen if the volcanic vent was temporarily blocked and the system pressurized, finally blowing out the blockage. They showed that particles rapidly settle to the floor to form a granular deposit while a dilute gas-particle mixture streams toward the dike-drift intersection along the drift ceiling. The calculations presented in section 7 extend the results of *Dartevelle and Valentine* [2005].

4. Model Assumptions

[14] There are three main underlying assumptions to our model of the interaction between fragmented flow of basaltic magma and repository drifts. First, and already mentioned in section 2, is that volcanic activity at the repository is most likely to be similar to that which is inferred to have occurred at the Quaternary volcanoes in the region based upon field studies. Data from older volcanoes in the region are also used as a basis for the geometry of that interaction because we can directly observe dikes and conduits at some of these eroded centers. Second, we assume that fragmented flow is an appropriate end-member for magma-drift interaction (the other end-member being flow of viscous, unfragmented magma into/out of drifts). For the water contents inferred for Quaternary volcanoes near Yucca Mountain, fragmentation under homogeneous flow conditions could occur at depths of $\sim$200–1000 m [*SNL*, 2007a], justifying the assumption of fragmented flow at repository depths as an end-member. The third fundamental assumption is that a multifield approach, wherein a continuous gas phase and a dispersed particle phase are treated as overlapping continua each satisfying mass, mo-

mentum and energy conservation, provides an accurate representation of the flow field [*Dartevelle*, 2005]. The multifield approach has been successfully applied to many pyroclastic systems (see reviews by *Valentine* [1998a] and *Dartevelle* [2004]), and the validation efforts summarized in section 6 provide confidence that the approach is appropriate for the problem at hand. Of course, there are many other assumptions regarding issues such as material properties, equations of state, and rheology, that are part of the model analysis here, but the three assumptions described above are the most fundamental for our approach.

5. Numerical Approach and Problem Setup

5.1. Computer Code

[15] For the modeling studies reported here we use GMFIX (version 1.62), which is a set of multiphase computational fluid dynamics codes that are derived from the MFIX family of codes [*Dartevelle*, 2004; *Symlal*, 1998; see also http://www.mfix.org] in order to model geophysical multiphase problems. The first applications of GMFIX to volcanological problems focused on full-scale Plinian eruption columns in the atmosphere and on the flow and deposition of pyroclastic density currents [*Dartevelle et al.*, 2004]. *Dartevelle* [2006a, 2006b, 2006c, 2007] provides a detailed description of the physical models and numerical solution techniques in GMFIX 1.62, as well as a user manual. Table 1 describes the numerical properties used.

5.2. Problem Geometry and Boundary Conditions

[16] Our focus is on transport processes between the plumbing of a small monogenetic volcano and repository openings in the fragmented flow regime. As described in section 2, at repository depths the volcanic plumbing is characterized by vertical or subvertical dikes on the order of meters in width that are most likely to have strikes oriented at high angles to repository drifts. For the model calculations presented in section 7, we approximate this geometry in two-dimensional Cartesian coordinates (Figure 3). The problem setup can be thought of as a vertical plane through the centerline of a drift and a vertical dike that is orthogonal to the drift (Figure 4); this setup models the drift as a horizontal sheet and assumes there are no gradients in transport properties in the third dimension. Clearly, this is a simplification compared to the real three dimensionality of the problem, which would more realistically have a vertical dike intersecting a horizontal tube. The simplification is necessary for the practical reason that it allows us to conduct a range of these computationally intensive simulations. As stated in section 1, our goal is to understand the basic processes and ranges of parameter values for generalized magma-repository interactions, rather than to predict exactly what might happen in a detailed 3-D sense for a specific scenario. We expect that the general transport phenomena that would occur in a 3-D drift are similar, at least along the vertical center plane of the drift, to those that are captured in the 2-D simulations, although the presence of waste packages and drip shields (which occupy $\sim$20% of the cross-sectional area of a drift; see Figure 2b) would complicate the details of the flow field through drag and geometric effects. Details of the numerical grid are provided in Table 2.
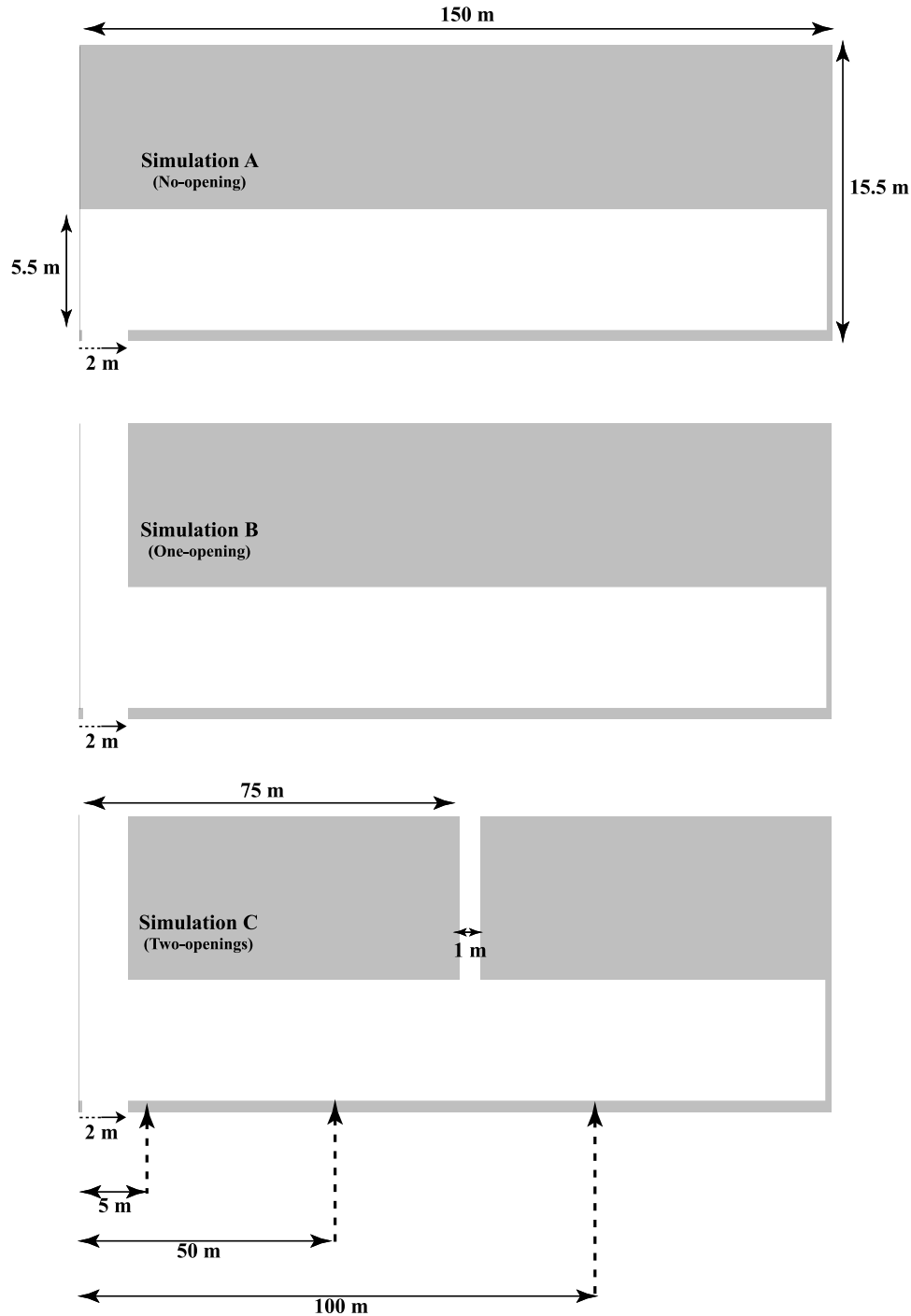
Figure 3. Simulations A, B, and C depending on the number of exits to the surface. The dashed arrows at 2 m, 50 m, and 100 m indicate the locations of sampling. The gray area symbolizes a no-slip wall.

[17] The three problem geometries (Figure 3) all treat the left-hand boundary as a symmetry boundary (free slip), therefore the domains shown are half-space domains. The vertical dike width is 4 m, but only a 2 m width is simulated because of the problem symmetry. The 4 m width is within the range of dike widths observed in the field, as summarized in section 2, but smaller than the mean value of 8 m. For a given mass flux this means that the simulations in section 7 will have higher velocities than would be the case

with an 8 m feeder dike. GMFIX is strictly a hydrodynamics code and does not model the solid mechanics associated with opening a dike, making it necessary to assume that the vertical pathway is already completely open at the initiation of a simulation. The horizontal drift is 5.5 m high. Flow enters the domain at the inlet at the bottom of the vertical dike (see section 5.3). Geometry A (Figure 3, top) considers a case where the dike does not extend above the drift. This provides an extreme case where all the rising mass is
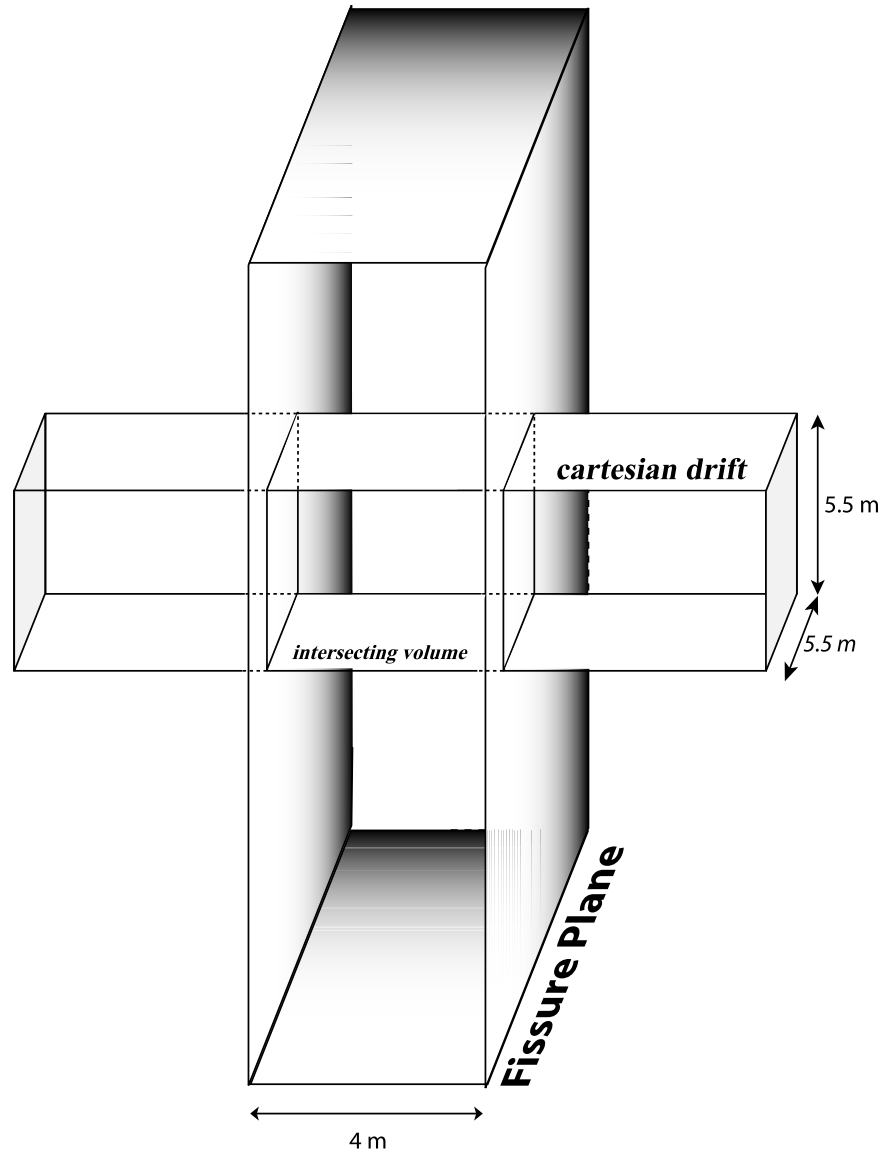
Figure 4. Perpendicular intersection between an ideal Cartesian rectangular drift tunnel of dimension of 5.5 × 5.5 m and a fissure plane with a width of 4 m. At the inlet, the eruptive working surface area is 4 × 5.5 m = 22 m^2.

diverted laterally into the drift. Geometry B (Figure 3, middle) is the most realistic geometry, in which the dike continues above the drift and outflow is allowed at its top. Geometry C (Figure 3, bottom) is similar to B except that a secondary vertical dike that allows outflow extends upward from the drift at a horizontal distance of 75 m from the main feeder dike. As discussed in section 3.2, we consider the formation of such a secondary dike to be unlikely based upon analyses from *BSC* [2004b] but have performed simulations in order to understand what the effects might be on the flow field. The secondary dike in geometry C is 1 m wide. Outlet pressures are held at 0.1 MPa (atmospheric pressure), which probably draws mass out of the domain faster than would occur in reality where the pressure would decrease more gradually with height in the dike(s) above the repository. Except for the left-hand boundary, the inlet, and the outlets (geometries B and C), all other boundaries have a no-slip condition in all of the simulations.

5.3. Initial Conditions and Boundary Conditions at the Inlet

[18] Initial conditions for most of the calculations have the domain filled with air at atmospheric pressure (reflecting good connection between repository depths and the

Table 2. Geometry for All Simulations

Parameter	Value
Horizontal length X (m)	150
Horizontal resolution ΔX (m)	0.5
Number of grid points in the X direction	305
Vertical length Y (m)	19
Vertical resolution ΔY (m)	0.5
Number of grid points in the Y direction	39
Drift height (m)	5.5
Inlet (dike) width (m)	2.0
Main outlet width (dike for simulation B and C) (m)	2.0
Secondary outlet width (fracture for simulation C only) (m)	1.0

Table 3. Physical Properties at the Inlet for All "Magma Filling" Simulations

	High Vapor Content (Hwv)	Low Vapor Content (Lwv)
The total mass fraction of water (wt %)	4.6	1.2
Volumetric solid concentration[a] (vol %)	14.06	39.38
Mass flux per unit of length[b] (kg/s m)	8.4×10^3	8.4×10^3
Vertical speed (m/s)	5.7	2.11
Calculated mixture density (kg/m^3)	368.5	996.5
Calculated mixture speed of sounds[b] (m/s)	172.1	87.4
Calculated mixture static pressure[b] (Pa)	110.88×10^5	75.78×10^5
Calculated mixture specific heat ratio[b]	1.0160	1.0042

[a]It is worth noting the difference and similarity between these two flows: Hwv is a collisional somehow diluted flow, while Lwv is a much more concentrated flow. Yet both flows are in the collisional dissipation regime [*Dartevelle*, 2004].

[b]From *Dartevelle and Valentine* [2007a].

atmosphere via fracture porosity) and a temperature of 25°C. The inlet pressure is 12.5 MPa. This is toward the high end of magma pressures that might be expected in a volatile-rich basaltic dike, and represents an overpressure of 6 MPa (the maximum magma overpressure estimated by *BSC* [2004b], corresponding to the early repository thermal period; see section 3.1) and a lithostatic stress of 6.5 MPa (appropriate for repository depths and a bulk rock density of ~2200 kg/m^3). This initial high pressure contrast between the inlet and the flow domain will exaggerate early time processes. For example, a strong shock wave propagates rapidly from the inlet area into the drift. The occurrence of such shock waves was also modeled by *Woods et al.* [2002] and *Dartevelle and Valentine* [2005], but in reality the process of opening of a vertical dike will likely reduce the strength of such shocks and possibly eliminate them [*BSC*, 2004b]. In terms of impacts on waste packages, it is unlikely that the highly transient initial shocks, if they were to occur, would significantly damage intact waste packages. Rather, the most potentially damaging processes are related to the dynamic pressures and high temperatures caused by the ensuing pyroclastic flow [e.g., *Valentine*, 1998b]. In addition, initial accelerations of the rising gas-particle mixture will be exaggerated by the initial conditions that we apply. However, uncertainties in our knowledge of the detailed early pressure history of a rising pyroclastic mixture, when it encounters a low-pressure cavity, have led us to choose this relatively simple initial condition.

[19] Simulations were conducted with each geometry for two values of water content for the gas-particle mixture, namely, 4.6 wt % and 1.2 wt % (referred to as Hwv and Lwv cases, respectively; Table 3) representing the high and low ends of the water content spectrum for trachybasalts in the Yucca Mountain region (see section 2); we assume that at the shallow depths of interest the water is entirely present as a gas phase. The inflow velocities and particle concentrations were determined by the water contents, inlet pressure, and a mass flux per unit length (M_f) of ~8.4×10^3 kg/s m (this is a mass flux per unit length of dike in the direction orthogonal to the plane of the 2-D calculations). This corresponds to a total mass flux of 7.4×10^5 kg/s, the maximum anticipated for a potential future violent Strombolian eruption at Yucca Mountain [*SNL*, 2007a] focused along 90 m of dike length (encompassing one drift and

extending approximately to the midpoint of the intact host rock on either side of a drift). The vertical velocity of the gas-particle mixture is calculated with M_f, the mixture density for each volatile content (368.5 kg/m^3 for Hwv and 996.5 kg/m^3 for Lwv), and the dike width (w = 4 m; see Table 4), as

$$V_{mix} = M_f/(\rho_{mix}w)$$

With the resulting vertical speeds (5.7 m/s for Hwv and 2.11 m/s for Lwv), we note that both flows are largely subsonic; Lwv mixture vertical speed is 2.4% of its own sound speed, while Hwv vertical speed is 3.3% of its sound speed (the mixture speed of sound is calculated following *Dartevelle and Valentine* [2007a]). Given these low speeds, these flows are therefore mostly driven by the pressure differences between the drift and the inlet.

[20] Temperature of the gas-particle mixture at the inlet is 1373 K. The particle size of 100 microns (0.1 mm) used for most of the simulations corresponds to the estimated mean particle size for violent Strombolian eruptions [*SNL*, 2007a], noting, however, that there are few data that constrain this value (Table 4). Two simulations were conducted with a larger particle size (1 mm and 1 cm) in order to explore the effects of a lesser degree of fragmentation (Table 4). The inlet boundary conditions are provided in Tables 3 and 4. Additionally, simulations were conducted to explore the process of emptying of a drift, as might occur if a volcanic vent were temporarily blocked such that the underlying dike-drift system filled and pressurized and then was allowed to decompress when the blockage is blown out (Table 5).

6. Model Validation

[21] After thorough verification that GMFIX correctly solves the equations coded in it [*Dartevelle*, 2005, 2006a, 2007], there are two levels of model validation [*Dartevelle*, 2007; *Dartevelle and Valentine*, 2007a]: (1) validation that the numerical approach (the code implementation of a conceptual model) accurately represents the physical processes of compressible and turbulent multiphase flow as, for instance, measured in analog experiments [*Dartevelle*, 2007]; and (2) validation that our conceptual approach to setting up a simulation of a multiphase magmatic system interacting with a man-made opening, and the resulting simulations, result in phenomena that reasonably mimic that of a real event [*Dartevelle and Valentine*, 2007a]. Section 6.1 summarizes the verification and the validation against experimental data that the numerical code (GMFIX) has undergone. Section 6.2 summarizes a comparison of GMFIX model calculations with the 1977 eruption of tephra through a geothermal wellbore in Iceland that was intersected by a dike at a depth of ~1 km, which is the only example of basaltic magma interacting with a man-made opening that we are aware of. Both of these validation studies are reported in detail elsewhere (see *Dartevelle* [2007] and *Dartevelle and Valentine* [2007a], respectively).

6.1. Verification and Validation Against Analogs

[22] GMFIX (v1.62) is the code implementation of the conceptual multiphase Navier-Stokes model of *Dartevelle*

Table 4. Initial and Boundary Physical Properties for All "Magma Filling" Simulations

	Simulation		
	A (No Exit)	B (One Exit)	C (Two Exits)
Drift			
Pressure[a] (Pa)	1.01×10^5	1.01×10^5	1.01×10^5
Temperature[a] (K)	298.0	298.0	298.0
Calculated gas density (kg/m^3)	1.1845	1.1845	1.1845
Mass fraction of water in vapor phase[b]	0	0	0
Volumetric solid concentration[b] (vol %)	0	0	0
Kappa (gas phase turbulent production) (m^2/s^2)	0.01	0.01	0.01
Epsilon (gas phase turbulent dissipation) (m^2/s^3)	100.0	100.0	100.
Inlet			
Mixture temperature (K)	1,373	1,373	1,373
Gas pressure[c] (Pa)	125.0×10^5	125.0×10^5	125.0×10^5
Calculated gas density (kg/m^3)	19.726	19.726	19.726
Mass fraction of water in vapor phase[d]	1.0	1.0	1.0
Grain diameter[e] (m)	100×10^{-6}	$10^{-4}, 10^{-3}, 10^{-2}$	100×10^{-6}
Grain/magma density (kg/m^3)	2500	2500	2500
Theta, granular temperature (solid phase turbulent production) (m^2/s^2)	0.01	0.01	0.01
Solid inelastic collisional dissipation coefficient	0.9	0.9	0.9
Kappa (gas phase turbulent production) (m^2/s^2)	0.01	0.01	0.01
Epsilon (gas phase turbulent dissipation) (m^2/s^3)	100.0	100.0	100.0
Main Outlet			
Gas pressure[a] (Pa)	NA	1.01×10^5	NA
Gas temperature[a] (K)	NA	298.0	NA
Secondary Outlet			
Gas pressure[a] (Pa)	NA	1.01×10^5	1.01×10^5
Gas temperature[a] (K)	NA	298.0	298.0

[a]This corresponds to a standard atmosphere. NA, not applicable.
[b]This corresponds to an atmosphere of pure and clean dry air.
[c]This corresponds to lithostatic plus magmatic water vapor pressure.
[d]This corresponds to magma gas of pure water vapor.
[e]Simulation B (one exit) scenario has been performed with three different particle sizes (100 μm, 1 mm, and 1 cm) for the Hwv case.

[2005] and the multiphase turbulence model of *Simonin* [1996] [see also *Benyahia et al.*, 2005]. The numerical implementation of *Dartevelle*'s [2005] conceptual models into the GMFIX code has been extensively tested to ensure that the results of simulations are accurate representations of the physical systems modeled [*Dartevelle*, 2007]. First, the GMFIX code has been verified against ideal and analytical Riemann's shock tube test cases. *Dartevelle* [2007] showed that the numerical solvers and the spatial and time discretization methods implemented in GMFIX ensure the accuracy of the numerical solutions. In addition, it was shown that the numerical accuracy is independent on the grid size chosen even though, as expected, the quality of the numerical results decreases with coarser grid size. Second, the full model has been validated against previously published analog experimental data of overpressured pure gas and gas-particle jet dynamics and of particle-laden turbulent jets [*Ladenburg et al.*, 1949; *Lewis and Carlson*, 1964; *Hishida et al.*, 1987; *Viollet et al.*, 1992; *Dartevelle*, 2007]. The underexpanded jet analog validation test cases demonstrate the adequacy and the accuracy of GMFIX to capture single to multiphase dynamics under supersonic and shocked conditions. GMFIX accurately captures the shock disc positions, even with coarser grid resolutions [*Dartevelle*, 2007]. These tests also demonstrate the adequacy of the model for coupling between particles and gas phase through shocks. The turbulent particle-laden jets analog validation test cases tested the adequacy of the single and multiphase

Reynolds averaged Navier-Stokes (RANS) turbulence model [*Simonin*, 1996; *Benyahia et al.*, 2005]. Indeed, the dispersed phase has important effects upon the dynamical and turbulent development of a jet which must be captured

Table 5. Initial and Boundary Physical Properties for the "Pyroclast Emptying" Simulation

Parameter	Simulation B (One Exit)
Drift	
Pressure[a] (Pa)	125.0×10^5
Temperature (K)	1373.0
Calculated gas density (kg/m^3)	19.726
Mass fraction of water in vapor phase[b]	1
Volumetric solid concentration (vol %)	40
Mixture temperature (K)	1373
Grain diameter (m)	1×10^{-3}
Grain/magma density (kg/m^3)	2500
Theta, granular temperature (solid phase turbulent production) (m^2/s^2)	0.01
Solid inelastic collisional dissipation coefficient	0.9
Kappa (gas phase turbulent production) (m^2/s^2)	0.01
Epsilon (gas phase turbulent dissipation) (m^2/s^3)	100.0
Main Outlet	
Gas pressure[c] (Pa)	1.01×10^5
Gas temperature[c] (K)	298.0

[a]This corresponds to lithostatic plus magmatic water vapor pressure.
[b]This corresponds to fragmented magma gas and pure water vapor.
[c]This corresponds to a standard atmosphere.

Table 6. Inferred Time Scale for the Low Water Vapor and High Water Vapor Flows

Water Vapor Mass Fraction (wt %)	Vertical Speed of the Mixture V_{mix} (From Table 3) (m/s)	Inferred Time Scale $t_s = W/V_{mix}$ (s)
1.2 (Lwv)	2.11	0.948
4.6 (Hwv)	5.70	0.351

properly with a *multiphase* turbulence model. The RANS turbulence model in GMFIX couples production and dissipation of turbulence between the dispersed and the gas phase in solving three coupled scalar turbulence quantities [*Dartevelle and Valentine*, 2007a]. This coupled multiphase turbulence model merges together the classical Reynolds-averaged Navier-Stokes approach [*Benyahia et al.*, 2005] of gas turbulence with a kinetic-collisional-plastic model for the dispersed phase [*Dartevelle*, 2004]. Given the experimental errors, the numerical results (speed and kinetic turbulent energies) were generally good when compared with analog results, although *Dartevelle* [2007] showed that some of the observed discrepancies in the turbulent kinetic energy profiles could be improved in generalizing the turbulent model to a full four-scalar partial differential equation RANS model.

6.2. Comparison With Iceland Borehole Eruption

[23] During the night of 8 September 1977, a basaltic dike intersected a borehole at a depth of ∼1000 m in the Námafjall geothermal field, Iceland, and basaltic tephra erupted from the wellhead. According to *Larsen et al.* [1979], the eruptive event began with an audible explosion followed by an incandescent column 15−25 m high. As the column grew in width over a period of about 1 min, "sparks and cinders" were ejected and a constant roaring sound was heard. This was followed by a period of 10−20 min during which apparently no gas or particles were erupted but toward the end of which red flashes were observed. The final phase consisted of "a series of rapid explosions or shots of glowing scoria," wherein explosions were focused in groups of rapid succession, over a total of about 1 min. Flow velocities of 20−30 m/s were estimated by *Larsen et al.* [1979] on the basis of observed ejecta heights. The borehole itself suffered little damage and resumed steam production at a similar rate as before the eruption, suggesting that its geometry was not changed during the event.

[24] *Dartevelle and Valentine* [2007a] used GMFIX to model the borehole eruption using information such as average eruption velocity and particle size as reported by *Larsen et al.* [1979]. Numerical simulations produced wellhead phenomena very similar to those documented at the Námafjall event, namely, during the final phase which *Larsen et al.* [1979] describe as follows: "The final phase consisted of a series of very rapid explosions or shots of glowing scoria. A few groups of explosions were observed each consisting of several individual shots." This phenomenon appears to be caused by the formation of particle-rich slugs that form during ascent of the gas-particle mixture up the long borehole; each "shot" was the expulsion of a slug of incandescent clasts. The slugs tend to form in waves such that a group of closely spaced slugs was expelled followed by a short period of lesser eruptive activity before the next group arrived at the wellhead. Although the comparison between GMFIX model results and visual observations is only qualitative, the similarity between model and observed phenomena lends confidence to the application of the code to flows involving interaction of multiphase volcanic mixtures with underground openings.

7. Model Results

7.1. Dimensional Analysis

[25] Processed output data were of two kinds: (1) classic dimensional data such as gas pressure, gas density, multiphase dynamic pressure and (2) dimensionless data such as normalized values of mixture pressure, mixture dynamic pressure, and velocity. Particle volumetric concentration (ε_s) has no units but was also normalized by the initial volumetric concentration at the inlet in order to quantify the dilution (or concentration) factor as the flow proceeds through the drift. In order to perform a dimensional analysis, one must find reference time, length, mass, temperature scales, which are representative of the physical nature of the two different multiphase flows at the inlet: the high water vapor (Hwv) and the low water vapor (Lwv) content flows (Table 3).

[26] The temperature of the magmatic basalt (i.e., 1373 K, Table 4) was taken as a reference since all phases at the inlet are assumed in thermal equilibrium for both Hwv and Lwv. Knowing the density of the gas phase (Table 4) and the volumetric fraction of the solid phase (Table 3) for a given temperature, one can infer, at the inlet, the mixture reference density for both Hwv and Lwv cases as shown in Table 3. In the same vein, the solid volumetric concentrations, ε_s, are normalized to the inlet volumetric concentrations, namely, 14.1 vol % for Hwv flow and 39.4 vol % for Lwv. Ideally, one would want to relate the reference length scale to some physical properties of the flow at the inlet to fully capture the differences between Hwv and Lwv flows. In the absence of a well-defined inner length scale property (turbulence length scales would be ideal, but they are not well defined within the field of multiphase turbulence), the width of the inlet is chosen as the normalizing length reference. Once the length reference scale is defined, the time reference scale can be easily defined knowing the reference speed (i.e., $t_s \sim$ length/speed). Two speeds that represent inner properties of flows (Hwv versus Lwv) can be taken, either the speed of sound of that mixture or the vertical ejection speed at the inlet. The former speed would define the time needed for pressure waves in these mixtures to travel the full width of the inlet, the latter speed would define the time needed for a parcel of fluid to travel from end-to-end the full width of the inlet. Experience has shown that, in this context, both speeds could be equally used; hence we have chosen the simplest definition which is the vertical speed at the inlet defined from the mass flux, M_f, and the mixture density, ρ_{mix}. Hence, the time scales inferred for Lwv and Hwv flows are shown in Table 6. We note that these two timescales are very similar; there is only a factor 2.7 between Hwv and Lwv flows.

[27] Because dynamic pressure is an important variable to assess possible damage within the drift, we also normalized by a reference pressure scale representative of a bulk

property of the mixture flow. The dynamic pressure is defined as

$$P_{dyn} = \frac{1}{2}\ \rho_{mix}\ U_{mix}^2,$$

where U_{mix} is the mixture horizontal speed. The dynamic pressure is normalized to the mixture static pressure at the inlet, which is defined as:

$$P_{static,\ mixture} = \rho_{mix}\ a_{mix}^2\ \gamma_{mix},$$

where a_{mix} is the mixture (multiphase) speed of sound and γ_{mix} is the mixture specific heats ratio, both calculated at the inlet (see *Dartevelle and Valentine* [2007a] for how to calculate these thermodynamic variables).

7.2. Filling Scenarios

[28]   We describe first the simulations with the 100 μm particles for the three geometric scenarios, two exits (outlets) toward the surface (simulation C), one exit toward the surface right above the dike (simulation B), and no exit at all (simulation A). Although simulation C represents the most complicated of the three geometries, its dynamics are simpler and serve as a reference point for simulations with the other two geometries, and therefore, we discuss it first. In the ensuing discussion the term "down drift" refers to flows that move away from the main feeder dike (i.e., toward the right side of the computational domain), while "return flow" refers to motion toward the feeder dike (toward the left side of the domain).

7.2.1.   Flows With 100 μm Particles
7.2.1.1.   Simulation C: Two Exits

[29]   The second exit halfway down drift (e.g., see Figure 3, bottom) in the roof of the drift has an important effect upon the flow dynamics because it allows high backpressures, which otherwise would have increased at the end of the drift after the initial blast wave, to vent away (Movies 1 and 2). Consequently, the multiphase flow dynamics in this simulation are essentially dominated by the motion induced by the magma decompression at the inlet. This is a key difference with simulations A and B.

[30]   Most mass that is introduced at the inlet for the Hwv flow (initially 4.6 wt %) simply continues vertically up the main dike to exit the domain (Movie 1), but some is diverted and initially forms a dilute multiphase flow that flows along the drift roof (typical concentration ~1 vol %). As it reaches the end of the drift, it turns and moves back toward the main dike and forms a more concentrated granular flow (typical concentration ~10 vol %) on the floor of the drift. Eventually, this inbound flow is recycled within the dike with some material being diverted again to circulate through the drift and some leaving the system through the top of the feeder dike. Since this flow is only driven by the momentum gain by magma decompression at the source, it continues its recirculation pattern with no significant change of granular concentration. The Lwv (initially 1.2 wt %) has similar dynamics except at early times (Movie 2). Indeed, since this flow is relatively more particle enriched and therefore has more inertia (typical initial concentration at the roof ~10 vol %), it moves along the roof only about halfway down the drift (~80 m) to

eventually collapse and form a granular density current that continues to move down drift along the floor. Once this density flow splashes onto the end of the drift, it moves backward (sourceward) forming both a density current on the floor and a particle-gas cloud invading the whole drift (i.e., from floor to roof). Like the Hwv flow, this return flow will eventually be recycled within the dike.

[31]   Figure 5 shows dimensionless dynamic pressures sampled at different distances from the intersecting dike (2.5d, 25d, 50d) at 64 ut (unit of time). Figure 6 shows the equivalent dynamic pressures in SI units sampled 50 m away from the dike and at different times (10.5 s and 60 s). There are several interesting features from Figures 5 and 6: (1) for a given simulation (Hwv or Lwv), the dynamic pressures are self-preserving over the whole length of the drift (150 m) and over the whole time frame under consideration (1 min), typically ranging from 10^4 to 10^5 Pa or ~100 times less than the mixture static pressure at the inlet (Table 3); (2) there is essentially no significant difference between the dynamic pressures of Hwv and Lwv flows; (3) the highest dynamic pressures are on the roof and floor of the drift which are respectively subject to a hot buoyant flow on the roof and a return flow on the floor; and (4) the lowest dynamic pressures (~100 Pa) are halfway between the roof and floor reflecting the high shear between the down drift and return flow parts of the multiphase system (see horizontal speed profiles in Figure 9).

[32]   These are interesting features knowing that, at the inlet, the natures of these two flows (Hwv versus Lwv) are different to begin with; namely, Lwv is essentially a collisional granular flow, while Hwv is a turbulent kinetic dusty gas flow (Table 3) [*Dartevelle*, 2004]. However, one should remember that the effects of solid volumetric concentrations (39.4 versus 14.1 vol %, a factor ~2) upon the resulting dynamic pressures are countered by the difference between the vertical speeds at the inlet (2.11 versus 5.7 m/s, roughly also a factor ~2).

[33]   It is also interesting to capture the changes with time and space of the volumetric concentrations of solid particles. Figure 7 shows the variations of the solid volumetric concentration (Figure 7, left) and the ratio of volumetric solid concentration (Figure 7, right) sampled at different distances from the intersecting dike (2.5d, 25d, 50d) at time 64 ut, while Figure 8 shows the equivalent figure in SI units sampled 50 m away from the dike and at two different times (10.5 s and 60 s). The main features are that (1) for a given flow (Hwv or Lwv), the solid volumetric concentrations show little variation with time and space (Figures 7, left, and 8, left), ~1 to 10 vol % (kinetic-collisional type of granular flow [*Dartevelle*, 2004]; (2) consequently, the rate of dilution remains the same at any time everywhere, between 7 to 10 times less than the initial volumetric concentration at the inlet (Figures 7, right, and 8, right); and (3) as expected, Lwv (blue curve) shows higher particulate concentrations than Hwv.

[34]   Figure 9 shows the normalized mixture horizontal speed in the drift for both Hwv and Lwv flows sampled at various distance and at time 64 ut. At these times, both flows are subject to a return flow toward the inlet (negative speeds on the floor), while the roof of the drift is subject to a multiphase flow directed away from the main dike. One can see that the highest dilution rate (Figures 7b, 7d, and 7f) and
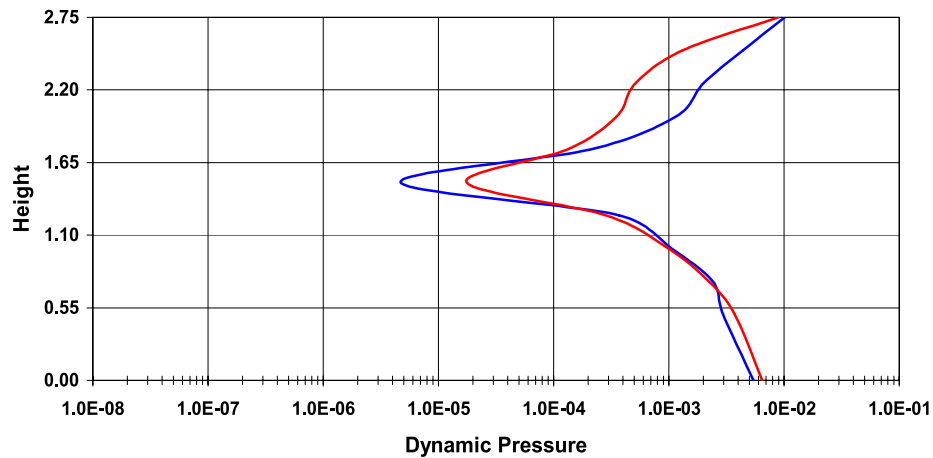
Dynamic pressure ratio at 2.5d and 64ut

A.

Dynamic pressure ratio at 25d and 64ut

B.
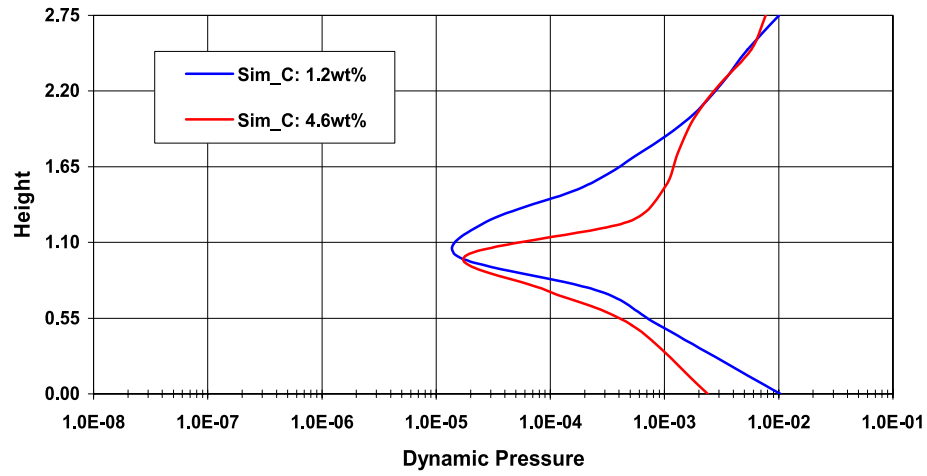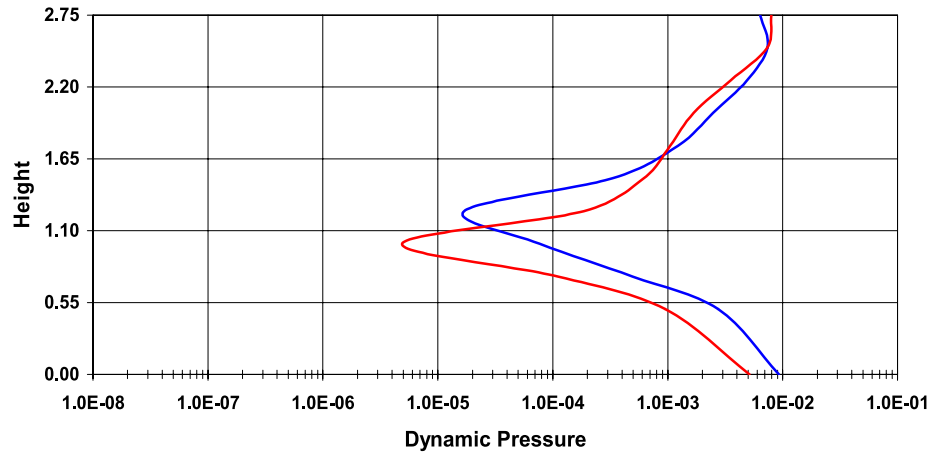
Dynamic pressure ratio at 50d and 64ut

C.

Figure 5. Dimensionless dynamic pressures for simulation C (two exits) sampled at a distance of (a) 2.5d, (b) 25d, and (c) 50d sampled at 64 ut. All axes are dimensionless; d is a dimensionless unit of length (normalized by the inlet width), and ut is a dimensionless unit of time defined from the mixture vertical speed.
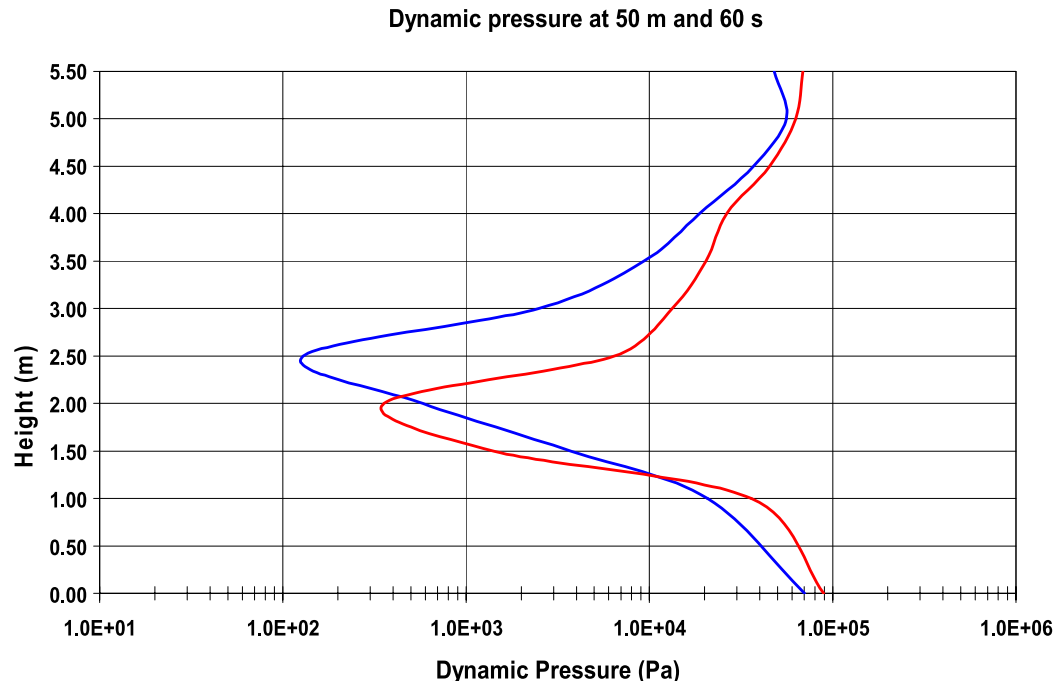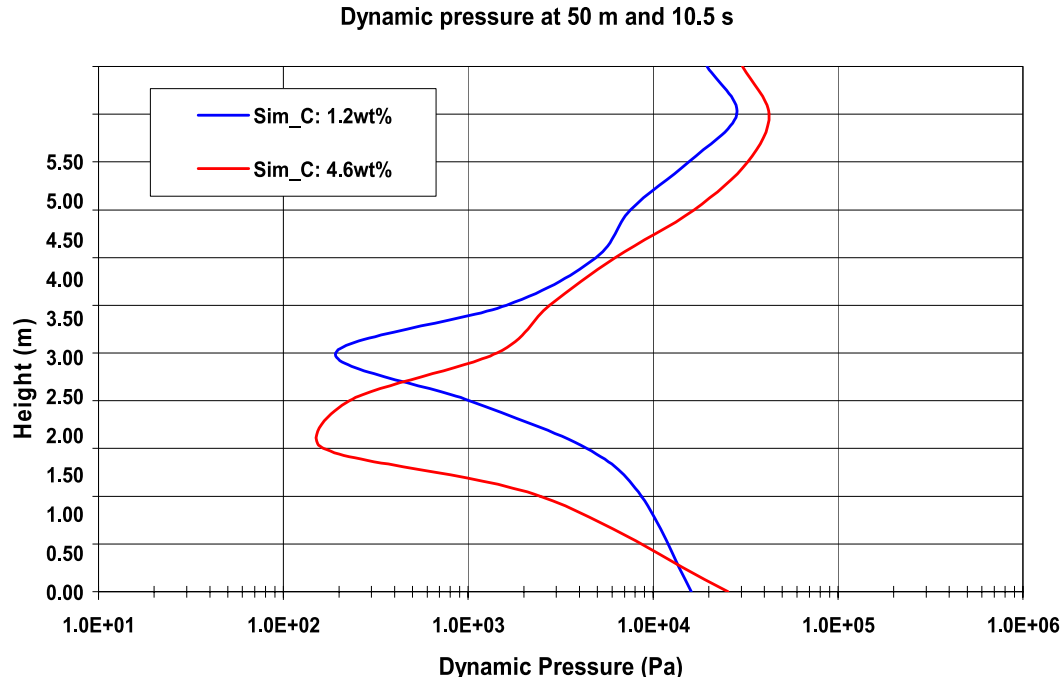
Dynamic pressure at 50 m and 10.5 s

A.

Dynamic pressure at 50 m and 60 s

B.

Figure 6. Dynamic pressures for simulation C (two exits) sampled at 50 m, at times (a) 10.5 s and (b) 60 s. Vertical axis is in m; horizontal axis is in Pa (log scale). The dynamic pressures for both Hwv and Lwv are remarkably similar, if not identical. Although the Lwv is more particle-rich, it nevertheless has, at the inlet, a ~3 times lower ejection vertical speed, hence globally traveling with much slower speed than the Hwv flow.

the lowest dynamic pressures (Figure 5) are between the roof and floor of the drift where the mixture horizontal momentum is minimal (Figure 9). This is consistent with *Dartevelle and Valentine*'s [2005] previous simulations.

[35] For both flows, the temperature varies little throughout the drift (~1373 K) during the time scale under consideration (1 min). It should be noted that the gas density for both Hwv and Lwv flows remains fairly constant throughout the whole drift. For instance, Table 7 shows the gas density sampled in two different locations in the drift at 10.5 s. After the first pressure wave released from the initial decompression at the inlet, there is a slight

A.
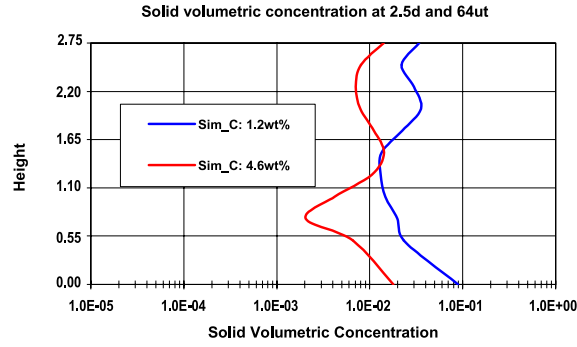
B.
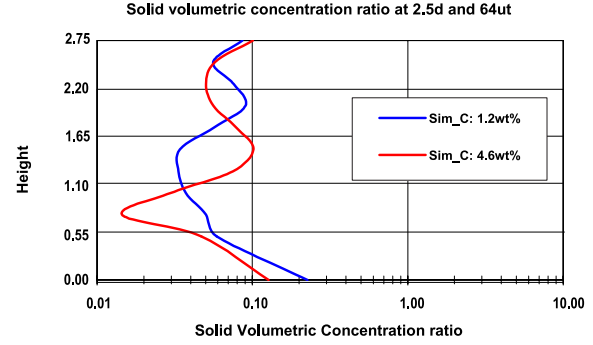
C.
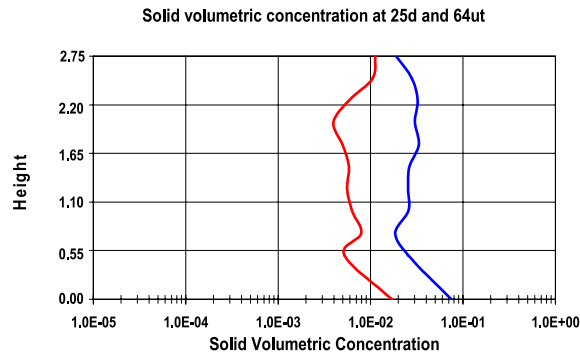
D.
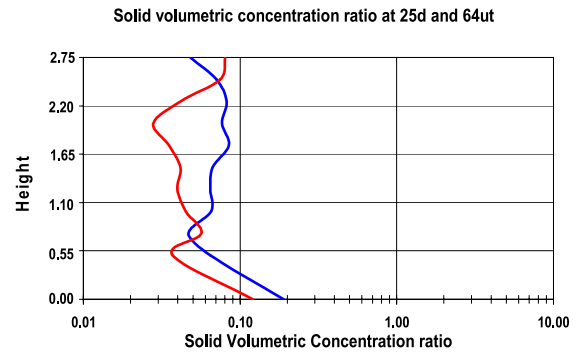
E.
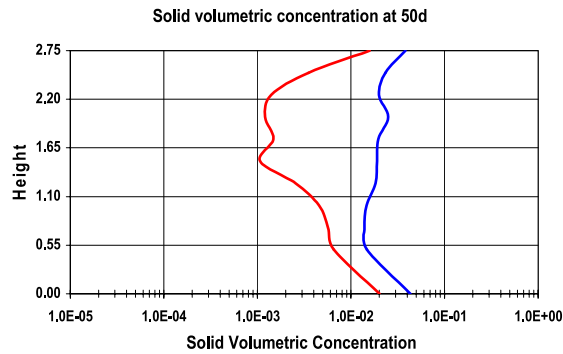
F.
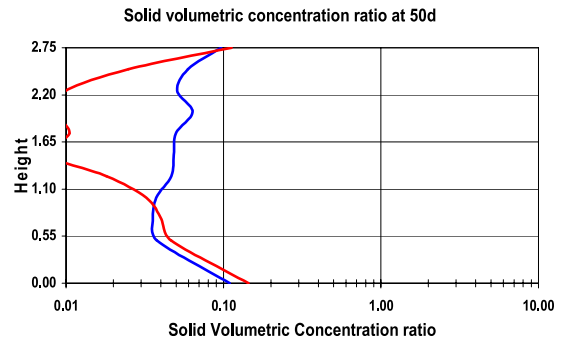
Figure 7. (left) Solid volumetric concentrations and (right) ratio of solid volumetric concentration (normalized by the concentration at the inlet) for simulation C (two exits) sampled at a distance of (a, b) 2.5d, (c, d) 25d, and (e, f) 50d and at time 64 ut. All axes are dimensionless; d is a dimensionless unit of length which has been normalized by the reference length scale (the inlet width), and ut is a dimensionless unit of time defined from the mixture vertical speed. From Figure 7 (left), it can be inferred that the solid concentration is always higher by about a factor of 10 for the Lwv flow (blue curve) than the Hwv (red curve). Both flows are diluted by a similar factor 10 as they travel down the drift tunnel (Figure 7, right).

increase of pressure in the right-hand side end of the drift (compare with simulation B).

7.2.1.2. Simulation B: One Exit

[36] Like simulation C, there is an exit toward the surface right above the main dike, yet, in this geometric configuration, this is the only pathway for the flow to leave the domain (Figure 3, middle). Because of this configuration, the flow dynamics are different than simulation C as mounting pressure at the end of the drift can eventually oppose the advancing multiphase flows within the drift: the flows are more diluted, subject to smaller dynamic pressures, and smaller horizontal speeds; particularly for the

Lwv flow which is also subject to a higher rate of sedimentation (Movies 3 and 4).

[37] Like in simulation C, the Hwv flow initially forms a slow, dilute multiphase flow along the drift roof (typical concentration ~1 vol %). As it reaches the end of the drift (Movie 3), it moves sourceward to form a gas-particle flow over the entire cross section of the drift (from floor to roof). Eventually, this return flow encounters the down drift flows midway in the drift, creating highly turbulent flows moving in both directions. As in simulation C, the more concentrated Lwv flow moves first on the roof to eventually (because the higher mixture density) collapse to the floor

A.
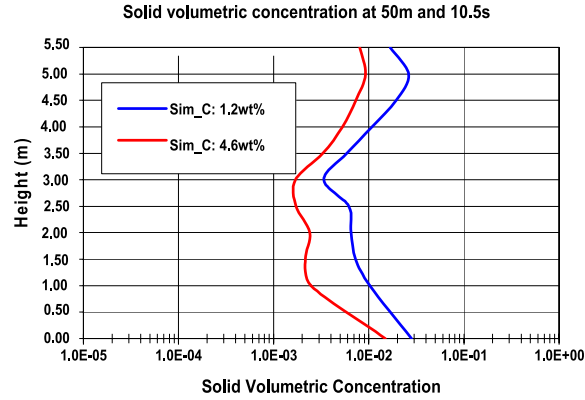
B.
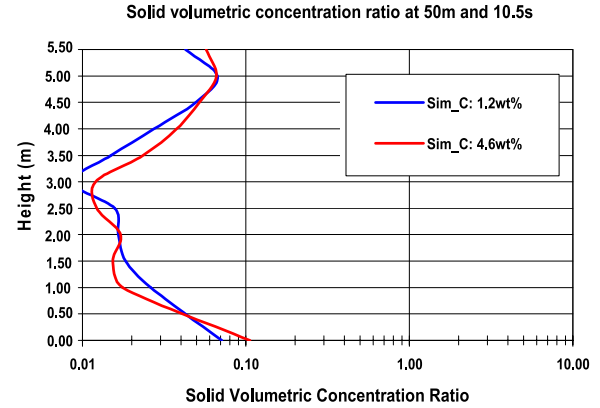
C.
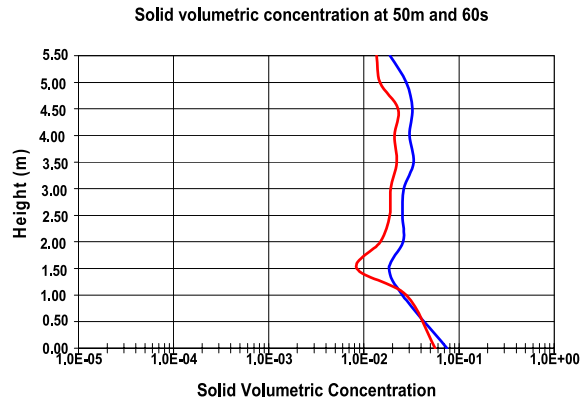
D.
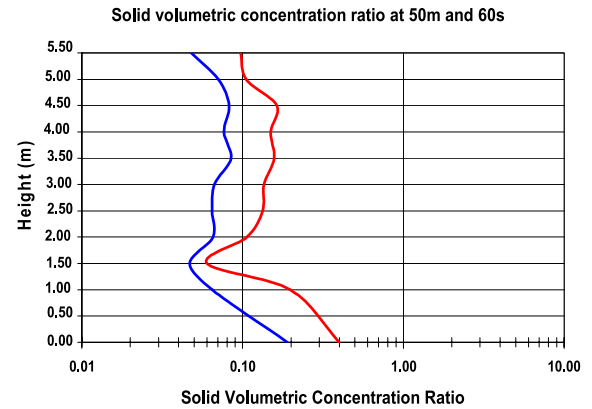
Figure 8. (left) Solid volumetric concentrations and (right) ratio of solid volumetric concentration (normalized by the concentration at the inlet) for simulation C (two exits) sampled at 50 m at times (a, b) 10.5 s and (c, d) 60 s. Vertical axis is in m; horizontal axis is dimensionless (log scale). Note that at these times, the solid volumetric concentration for the Lwv flow (blue curve) and Hwv (red curve) are very similar, if not identical, which indicates that Lwv is subject to a higher rate of dilution as shown in Figures 8b and 8d.

forming an outbound granular density current (Movie 4). Once that density flow encounters the end of the drift, it forms (unlike simulation C) a more concentrated granular density return flow on the drift floor (typical concentration ~1 to 5 vol %). Like Hwv flow, this return flow collides with the down-drift flow, creating a more complex multidirectional flow pattern with much smaller horizontal speeds than in simulation C.

[38] Figure 10 shows dimensionless dynamic pressures sampled at different distances from the intersecting dike (2.5d, 25d, 50d) and at 64 ut. Figure 11 shows the equivalent dynamic pressures in SI units sampled 50 m away from the dike and at different times (10.5 s and 60 s). Compared with Figures 5 and 6 of simulation C, there are clear and striking differences: (1) except perhaps at an early time, the dimensional dynamic pressures (Figure 11) are 1 to 2 orders of magnitude smaller than simulation C; this is even more exacerbated for Lwv flow (i.e., $10^2 - 10^3$ Pa for simulation B versus $10^4 - 10^5$ Pa for simulation C); (2) unlike simulation C, the Lwv and Hwv flows show important spatial (vertical) differences in their respective dynamic pressures; and (3) unlike simulation C, the Hwv flow loses most of its dynamic pressure (with respect to the mixture

static pressure at in the inlet) as it flows downstream. This is mostly due to the loss of momentum at the end of the drift (see Figure 14).

[39] Figure 12 shows the variations of the solid volumetric concentration (Figure 12, left) and the ratio of volumetric solid concentration (Figure 12, right) sampled at different distances from the intersecting dike (2.5d, 25d, 50d) and at time 64 ut. Figure 13 shows the equivalent figure in SI units sampled 50 m away from the dike and at two different times (10.5 s and 60 s). The following are the main features:

[40] 1. The solid volumetric concentration profiles are very different than those in simulation C, particularly for the Lwv flow, i.e., no solid material at the roof (except early in the simulation sequence, see, for instance, Figure 13a).

[41] 2. The important feature is that Lwv is only able to develop a granular flow on the floor of the drift but, unlike simulation C and Hwv flow, Lwv is unable to sustain a multiphase flow on the roof of the drift. Hwv flows maintain much longer a fully turbulent diluted flow over the whole height of the drift.

[42] 3. Like simulation C and only on the floor of the drift, the volumetric concentration for both Hwv and Lwv flows remains more or less constant, the order of 10^{-2} and

Mixture horizontal speed at 2.5d and 64ut

A.

Mixture horizontal speed at 25d and 64ut

B.

Mixture horizontal speed at 50d and 64ut

C.
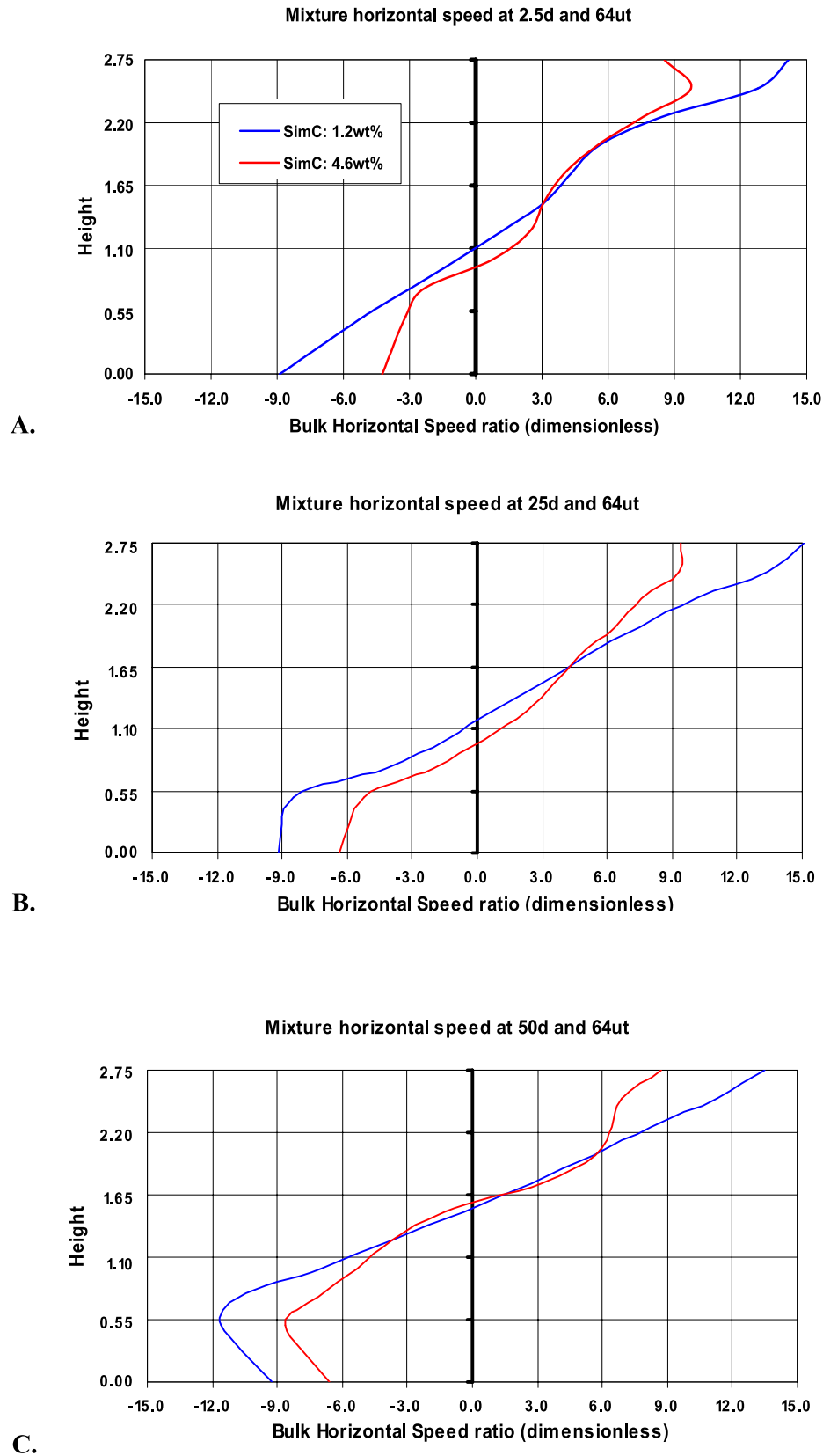
Figure 9. Dimensionless mixture horizontal speed for simulation C (two exits) sampled at a distance of (a) 2.5d, (b) 25d, and (c) 50d and at 64 ut. All axes are dimensionless; d is a dimensionless unit of length (normalized by the inlet width), and ut is a dimensionless unit of time. At 64 ut, all flows present little variations of horizontal speed. Note the inward buoyant multiphase flow at the roof and the backward granular flow (collisional dominated) flow on the floor.

Table 7. Gas Density Sampled at 10.5 s for Simulation C (Two-Exit Geometry)

Water Vapor Mass Fraction (wt %)	Averaged Gas Density (kg/m^3)	
	10 m Down Drift, 10.5 s	150 m Down Drift, 10.5 s
1.2 (Lwv)	0.34	0.69
4.6 (Hwv)	0.80	0.86

10^{-1} with a dilution factor of $\sim$10, however, slightly lower than in simulation C (compared with Figure 7 due to a net loss of particles).

[43] Figure 14 shows the normalized mixture horizontal speed in the drift for both Hwv (red curve) and Lwv (blue curve) flows sampled at various distance (2.5d, 25d, and 50d) and at time 64 ut (compared with Figure 9). Unlike simulation C, the speeds are small at the end of the drift. The velocity profiles for Hwv and Lwv are different, which is exacerbated because of the pressure difference between both ends of the drift. Indeed, in this simulation, very early on, there is an important gas pressure (or gas density) imbalance between both ends of the drift, especially for the Lwv flow. For instance, Table 8 shows the gas density sampled in two different locations in the drift at 10.5 s. Clearly, such a strong pressure unbalance (high pressure on the right hand-side of the drift, low-pressure on the left-hand side) promotes a return current (toward the dike and the exit) that the Lwv flow cannot oppose (particularly on the roof of the drift) and therefore most of the dusty materials on the roof are pushed backward, leaving only a multiphase flow moving down drift on the floor (Figure 12b). This explains the somewhat different concentration and dynamic pressure profiles than those in simulation C (lower dynamic pressures and lower solid particulate concentrations).

7.2.1.3. Simulation A: No Exit

[44] In this case, the drift is totally enclosed with no exit toward the surface (Figure 3). Like simulation B for the Lwv case, this configuration allows an unbalanced pressure configuration between the ends of the drift, which eventually hampers the propagation of the buoyant dusty flow on the roof and enhances the sedimentation of granular material onto the floor to even a quasi-granular deposit at the end of the drift (Movies 7 and 8).

[45] Overall, the flow dynamics are similar to simulations B and C. The Hwv flow initially forms a dilute multiphase flow moving down drift along the roof (typical concentration $\sim$1 vol %). As it reaches the end of the drift (Movie 7), it returns and forms a more concentrate granular flow (typical concentration $\sim$10 vol %) on the floor of the drift. Eventually, this return flow is recycled into the dike. Since no material can leave this system, the granular concentrations in the recirculating system increase with time. The Lwv has somewhat similar dynamics to simulations B and C. That is (Movie 8), since this flow is relatively particle enriched (i.e., more inertial, with initial concentration at the roof of $\sim$10 vol %), it only moves down drift on the roof a distance of $\sim$100 m to eventually collapse to the floor forming a down-drift granular density current. Once that density flow encounters the end of the drift it returns forming both a density current on the floor and a gas-particle cloud invading the whole drift (e.g., from floor to

roof). Like the Hwv flow, this return flow is eventually recycled within the dike but since no material leaves the system, concentration increases rapidly to gradually form a granular deposit starting at the end of the drift.

[46] Figure 15 shows dimensionless dynamic pressures sampled at different distances from the intersecting dike (2.5d, 25d, 50d) and at 64 ut. Figure 16 shows the equivalent dynamic pressures in SI units sampled 50 m away from the dike and at different times (10.5 s and 60 s). The key features to be noted are as follows:

[47] 1. Simulation A generates the highest absolute dynamic pressures (an order of magnitude higher than the maximum dynamic pressures of simulation C), $\sim$10^4–10^5 Pa for Lwv and >10^5 to >10^6 Pa for Hwv (Figure 16).

[48] 2. Like simulation B, the dynamic pressures tend to be smaller for Lwv flow than Hvw. However, further downstream in the drift (Figure 15c), Lwv and Hwv have very different sharply different pressure profiles.

[49] 3. At the end of the drift, Lwv flow generates a small dynamic pressure (see Figure 15c) which is due to the formation of a low-velocity, near plastic granular flow (e.g., Figure 17e, blue curve).

[50] Figure 17 shows the variations of the solid volumetric concentration (Figure 17, left) and the ratio of volumetric solid concentration (Figure 17, right) sampled at different distances from the intersecting dike (2.5d, 25d, 50d) and at 64 ut. Figure 18 shows the equivalent figure in SI units sampled 50 m away from the dike and at two different times (10.5 s and 60 s). The main features are that (1) like simulations B and C, the Lwv flow tends to form higher solid concentration flows than the Hwv flow (blue curve, Figure 17, left), except at the roof (Figure 17e); (2) Figure 17e indicates that Lwv develops the most concentrated flow of all simulations, $\varepsilon_s \sim$ 50 vol %, that is, dynamically speaking, at the onset of plasticity (frictional granular flow) [*Dartevelle*, 2004]; and (3) unlike simulations B and C, over 1 min, both Lwv and Hwv flows develop sedimentation patterns on the floor of the drift, i.e., with respect to the initial concentration at the inlet, the particle concentrations tend to increase rather than to decrease (e.g., Figure 17f compared with Figures 7f and 12f).

[51] Figure 19 shows the normalized mixture horizontal speed in the drift for both Hwv and Lwv flows sampled at various distance and at time 64 ut. At that time and like simulation C (Figure 9), Hwv is clearly subject to a return flow toward the inlet (negative speeds on the floor), while the roof of the drift is subject to a hot buoyant down-drift flow. However, unlike simulation C (Figure 9), Lwv flow shows a very different pattern further downstream in the drift. Indeed, because of early pressure differences between both ends of the drift in the Lwv case (as shown, for instance, in Table 9), Lwv cannot sustain a buoyant flow on the roof and instead forms a downstream granular flow on the floor (see Figure 19b and compare with Figure 9b), which becomes a slow plastic granular flow (Figures 19c and 17e) first and eventually an idle granular deposit at the end of the drift.

7.2.2. Flows With 1 mm or 1 cm Particles

[52] These simulations were performed with a single-exit geometry (simulation B) with a high water vapor content,
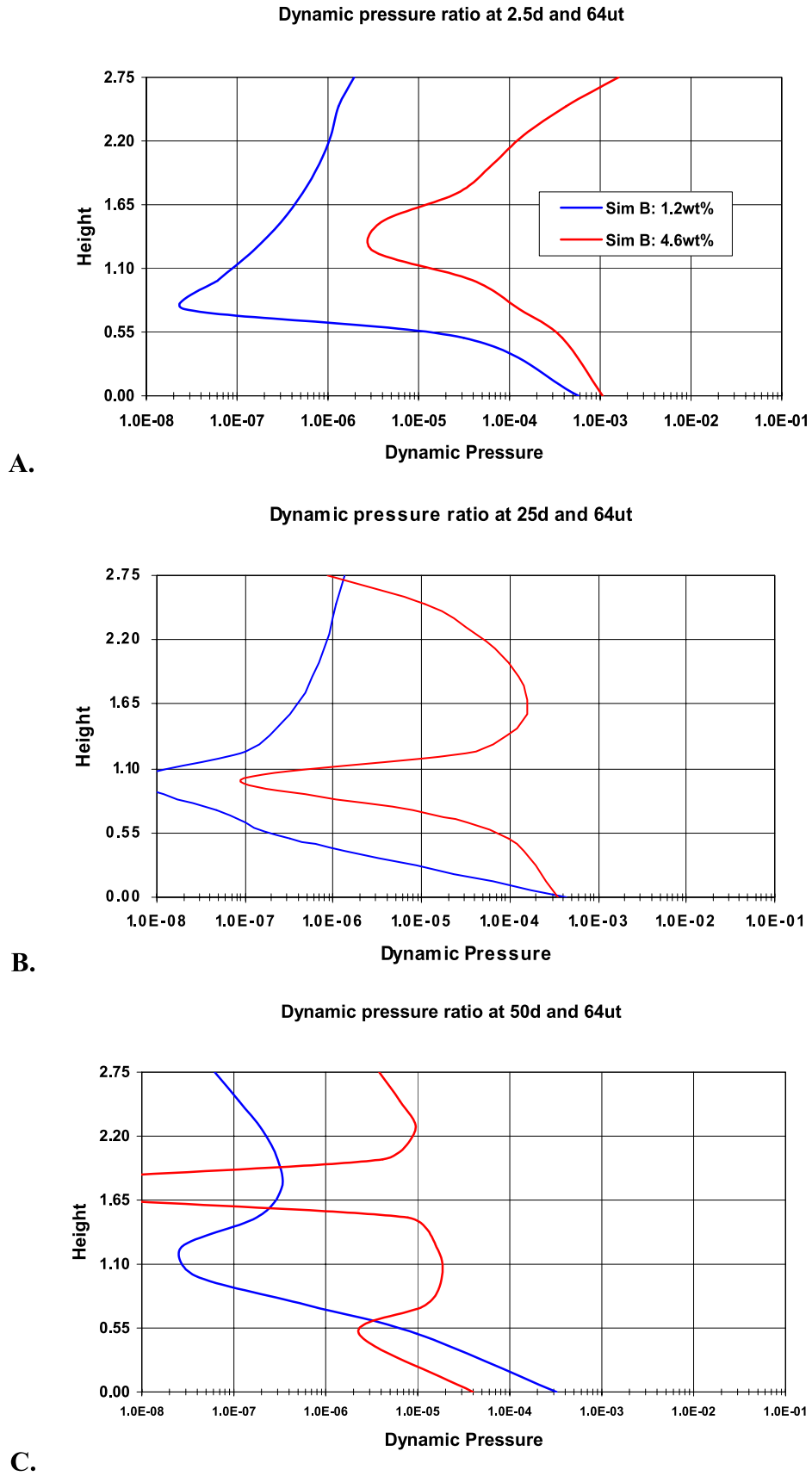
Dynamic pressure ratio at 2.5d and 64ut

A.

Dynamic pressure ratio at 25d and 64ut

B.

Dynamic pressure ratio at 50d and 64ut

C.

Figure 10. Dimensionless dynamic pressures for simulation B (one exit) sampled at a distance of (a) 2.5d, (b) 25d, and (c) 50d and at time 64 ut. All axes are dimensionless; d is a dimensionless unit of length (the inlet width), and ut is dimensionless units of time. Compare with Figure 5.
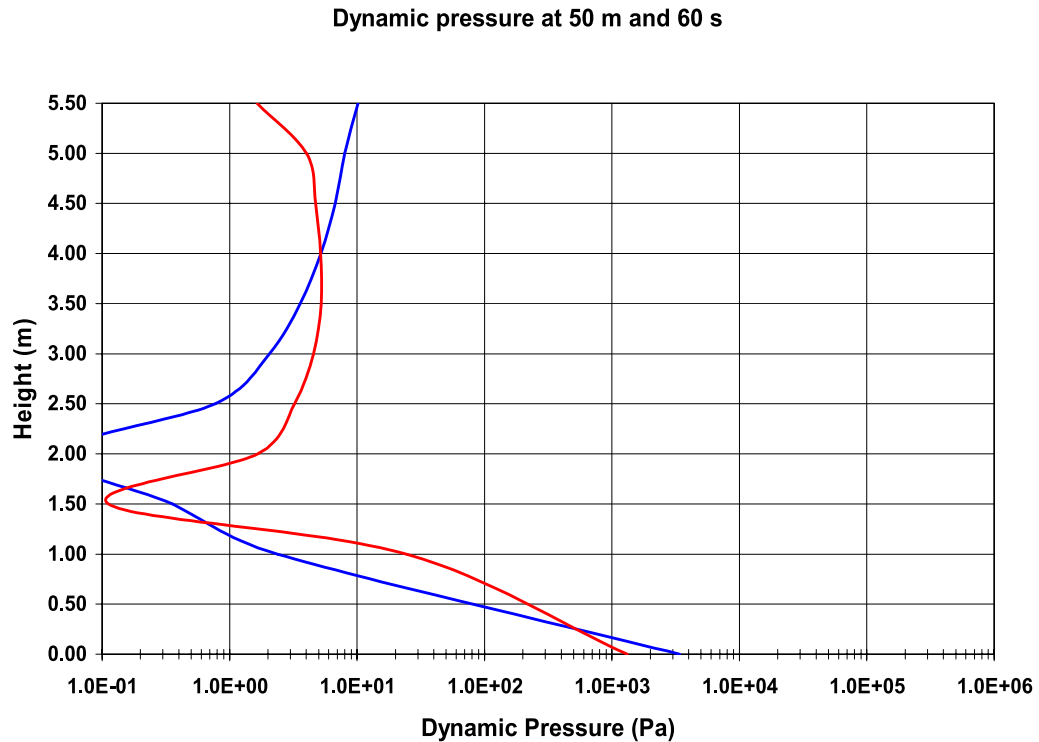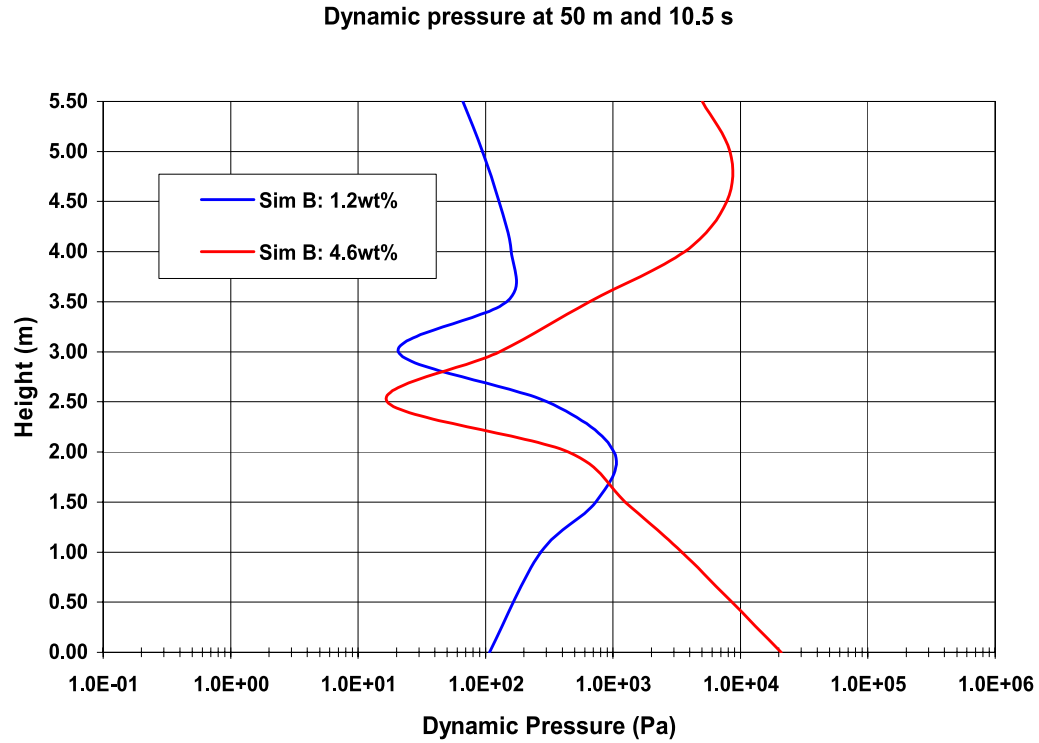
Dynamic pressure at 50 m and 10.5 s

A.

Dynamic pressure at 50 m and 60 s

B.

Figure 11. Dynamic pressures for simulation B (one exit) sampled at 50 m, at times (a) 10.5 s and (b) 60 s. Vertical axis is in m; horizontal axis is in Pa (log scale). Unlike simulation C, the dynamic pressures for Hwv and Lwv flows are very different. The main feature is that, initially, Lwv flow has the lowest dynamic pressure. When compared with Figure 6 (simulation C with two exits), the dynamic pressures in this one-exit scenario are 1 to 2 orders of magnitude smaller. This is due to a generation of less concentrated granular flows.

A.
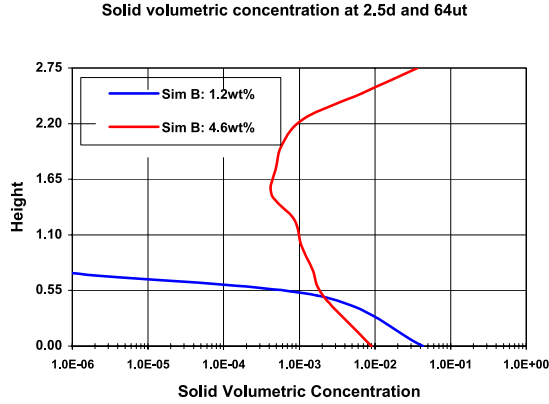
B.
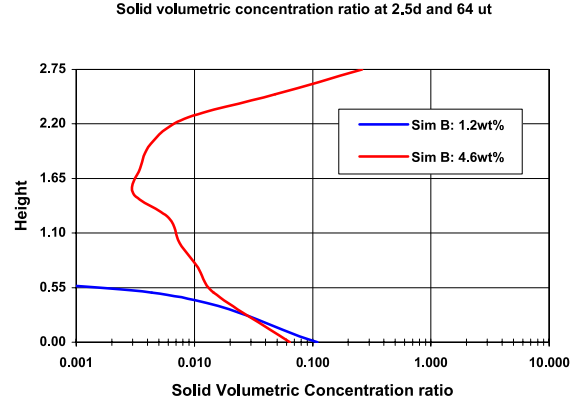
C.
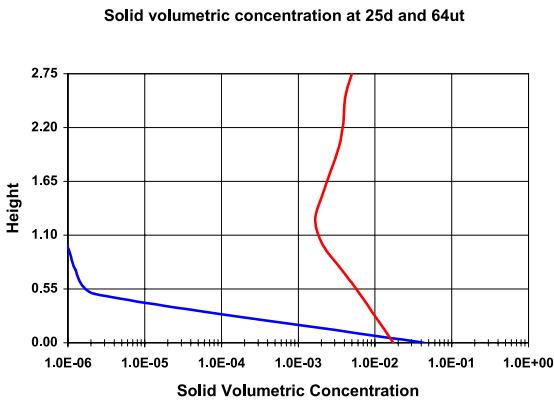
D.
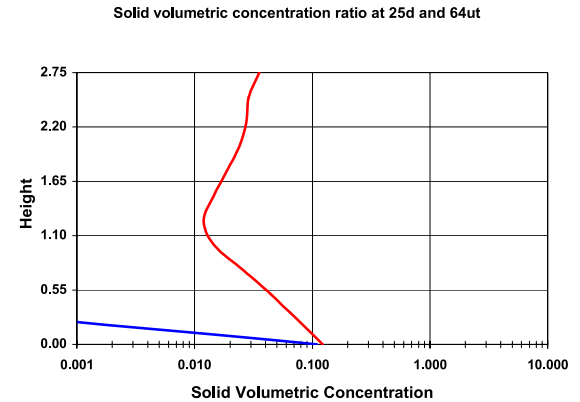
E.
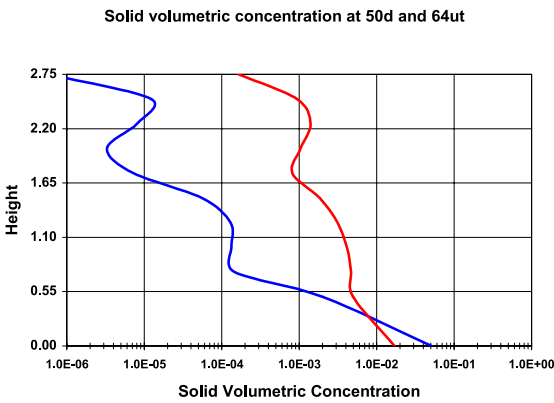
F.
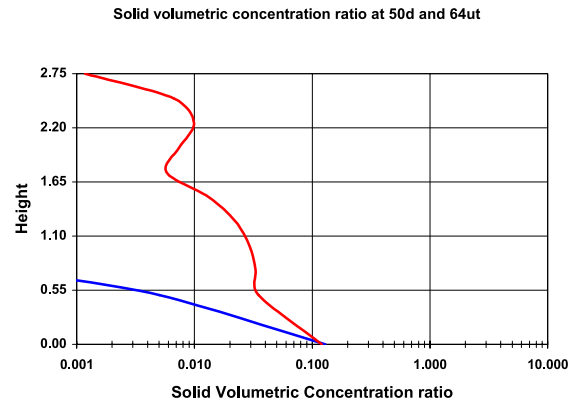
Figure 12. (left) Solid volumetric concentrations and (right) ratio of solid volumetric concentration (normalized by the concentration at the inlet) for simulation B (one exit) sampled at a distance of (a, b) 2.5d, (c, d) 25d, and (e, f) 50d and at 64 ut. All axes are dimensionless; d is a dimensionless unit of length (the inlet width), and ut is a dimensionless unit of time. Compared with Figure 7 (simulation C), in this case, Lwv flow is unable to develop a particle-rich flow on the roof.

4.6 wt % (Hwv flow) and with larger particle sizes; namely, 1 mm (Movie 5) and 1 cm (Movie 6).

[53] The flow dynamics are somewhat similar to the simulation B −4.6 wt % flow, except that because the particles are so much heavier (less well coupled to the gas phase), the flow collapses very quickly to the floor of the drift (∼50–70 m) to form a down-drift, concentrated granular flow on the floor of the drift (∼20 vol %). As the granular mixture reaches the end of the drift, it forms a

A.
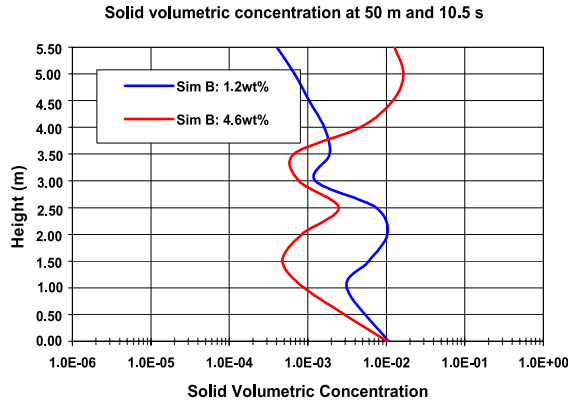
B.
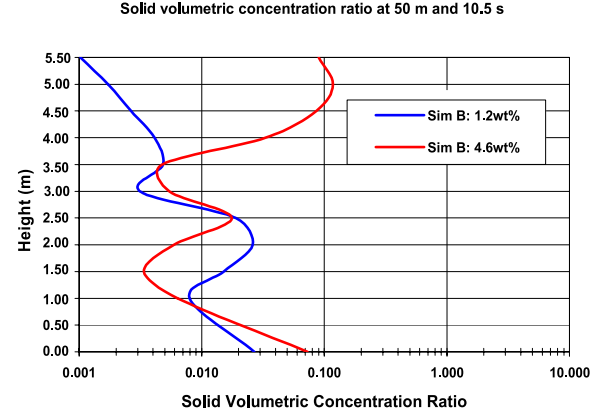
C.
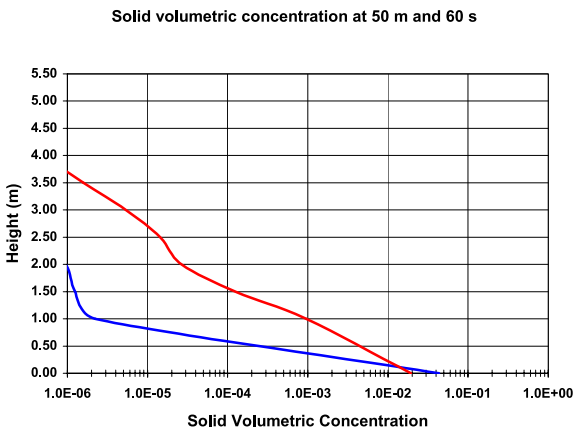
D.
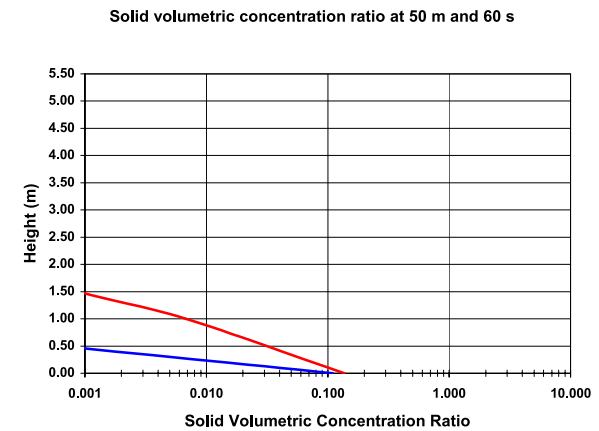
Figure 13. (left) Solid volumetric concentrations and (right) ratio of solid volumetric concentration (normalized by the concentration at the inlet) for simulation B (one exit) sampled at 50 m at times (a, b) 10.5 s and (c, d) 60 s. Vertical axis is in m; horizontal axis is dimensionless (log scale). When compared with Figure 8 (simulation C with two exits), it is interesting to note that this one-exit scenario generates a flow much more diluted (and even absent on the roof) and with smaller dynamic pressure.

granular deposit against the wall and then, by progressive aggradation, as more and more material arrives, the building of the granular deposit aggrades sourceward. This behavior is similar to that found by *Dartevelle* [2004] and *Dartevelle and Valentine* [2005].

[54] Figure 20 (sampled at 10 m in the drift), Figure 21 (sampled at 50 m), and Figure 22 (sampled at 100 m) compare the results obtained after 18.25 s of simulation for three different particles sizes (100 μm, 1 mm, and 1 cm). Figures 20 (left)–22 (left) represent the volumetric concentration and Figures 20 (right)–22 (right) represent the dynamic pressure. Because dynamic pressure also depends on the speed of the mixture [*Valentine*, 1998b; *Dartevelle and Valentine*, 2005], Figure 23 represents the mixture speed ratio (normalized by the speed at the inlet) sampled at 18.25 s and 50 m in the drift for these three different particle size flows (100 μm 23A, 1 mm 23B, and 1 cm 23C).

[55] Close to the inlet (Figure 20), there is no significant solid volumetric concentration difference between the different grain size simulations ($\sim$1 vol % on the floor), and each flow is well homogenized from floor to roof at this point. However, there is a clear effect of the particle size in

the dynamic pressure profiles, namely, the least inertial particles (100 μm) move laterally the fastest and therefore generate the highest dynamic pressure (10^4 Pa), while the most inertial (1 cm) are slower to be laterally displaced and therefore generate very small dynamic pressures (10 Pa), reflecting the sensitivity of dynamic pressure to the square of velocity. As the flow moves downstream in the drift (Figures 21 and 22), the 1 mm and 1 cm particles settle rapidly on the floor to form a denser collisional concentrated granular flow ($\sim$10 to 30 vol %), counteracting the effect of the low velocity and dramatically increasing the dynamic pressures to $\sim$$10^4$ Pa, while the flow with fine particles remains fairly diluted ($\sim$1 vol %) by turbulence throughout the drift, maintaining a relatively high-speed return flow with relatively constant dynamic pressures (10^3–10^4 Pa).

[56] Figure 23 clearly shows the dependency of mixture speeds on particle sizes. The fastest and most sheared flow has the smallest particles (Figure 23a). De facto, this low-inertial particle flow is subject to down-drift flow at the roof and return flow on the floor (with speed as high as 20.52 m/s), while the high-inertial particle flows are still moving down drift at speeds close to the initial inlet speeds ($\sim$5.7 m/s).

Mixture horizontal speed at 2.5d and 64 ut

A.

Mixture horizontal speed at 25d and 64 ut

B.

Mixture horizontal speed at at 50d and 64 ut

C.
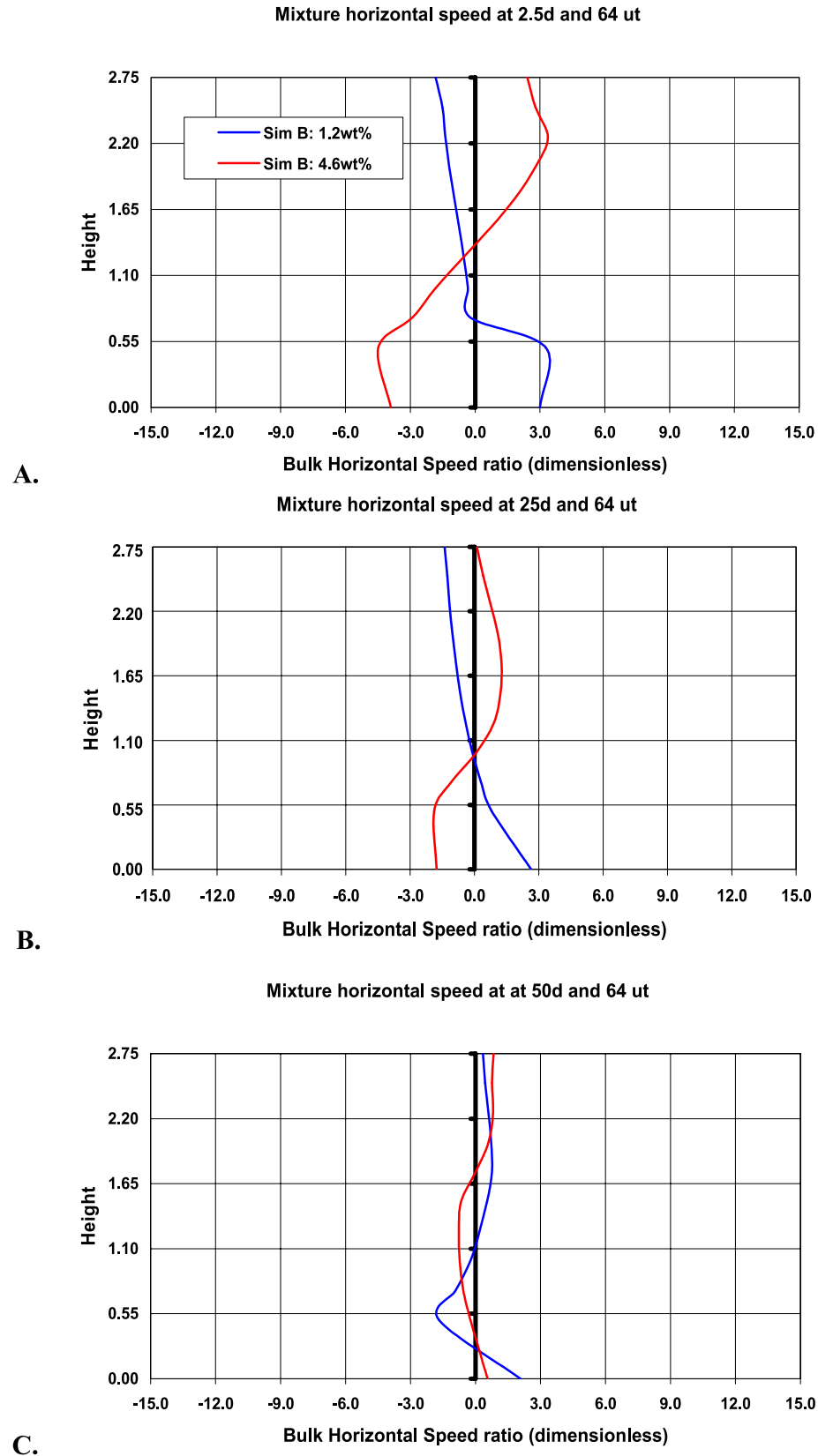
Figure 14. Dimensionless mixture horizontal speed for simulation B (one exit) sampled at a distance of (a) 2.5d, (b) 25d, and (c) 50d and at 64 ut. All axes are dimensionless; d is a dimensionless unit of length (normalized by the inlet width), and ut is a dimensionless unit of time. Compare with Figure 9. Although the absolute values of speed are similar for both Hvw (red curve) and Lwv (blue curve) flows, only Hwv develops a full downstream dusty flow on the roof and an upstream flow on the floor.

Table 8. Gas Density Sampled at 10.5 s for Simulation B (One-Exit Geometry)

Water Vapor Mass Fraction (wt %)	Averaged Gas Density (kg/m^3)	
	10 m Down Drift, 10.5 s	150 m Down Drift, 10.5 s
1.2 (Lwv)	0.60	2.37
4.6 (Hwv)	1.34	1.43

Hence one must conclude that low and high inertial particles, further downstream, generate the same dynamic pressures but for different reasons; namely, high inertial particles form a relatively slow high-density granular flow on the floor, while low inertial particles form a faster diluted flow (Figures 23 and 21).

7.3. Emptying Scenario

[57] This simulation explores the sudden decompression of a pyroclast-filled dike-drift system as might occur following the failure of a magma plug in the overlying volcanic vent area (Movie 9). The configuration is the same as the one explored by *Dartevelle and Valentine* [2005] but with larger particles (1 mm instead of 100 μm as in the work by *Dartevelle and Valentine* [2005]) (see Table 5). Initially, the drift is filled with pyroclastic materials with a volumetric concentration of 40 vol % under a pressure of 12.5 MPa (Table 5). The decompression (the upper dike boundary is at a pressure of 0.1 MPa), creates a rarefaction wave that propagates into the pyroclastic material. Hence, the material progressively moves out from the drift into the dike but at the same time pyroclasts settle to the drift floor. In Figures 24c and 24d at 5 s and 50 m down the drift, the concentration at the roof is $\sim 10^{-5}$ vol % with horizontal speed of ~ -72 m/s, while at the floor level, concentrations are ~ 59 vol %, comprising a frictional (plastic) pyroclastic flow with speed of -3.6 m/s. At 10 s and at the same location (Figures 25c and 25d), there is a quasi <1 m thick granular deposit (the horizontal speed is ~ 0 m/s on the floor) and the upper part of the drift is being cleared of any residual pyroclasts (Figure 25c). Over 10 s of simulation, the maximum dynamic pressure encountered in the drift is $\sim 10^6$ Pa. These results are consistent with the previous work of *Dartevelle and Valentine* [2005] with 100 μm diameter particles.

8. Implications

[58] Before summarizing the results it is useful to consider the limitations and uncertainties in the modeling approach. As described in section 5, there are several important simplifications made in the model, including the simplifications of a 3-D problem into a 2-D computational domain and the initial and boundary conditions that tend to exaggerate some aspects of the flow. There are many uncertainties in the details of interaction scenarios, such as the range of possible dike sizes and orientations, the pressure in a dike and how the solid mechanics aspects of holding a dike open couple with fluid mechanics of a compressible multiphase mixture and flow into or out of a large void space, and the effects that waste packages and debris might have on the flow field. The purpose of our modeling is to understand the range of processes and parameter values (e.g., dynamic pressure and temperature) that might occur in the end-member behavior of interaction of a gas-particle mixture under relatively high pressure with an underground opening, rather than detailed interactions of a given scenario, and we suggest that the geometry and boundary conditions that we have used give us that level of information.

[59] We have explored different plausible scenarios over different geometry setups (i.e., one exit, two exits, or no exit to the surface), boundary conditions at the inlet (e.g., water content, 4.6 versus 1.2 wt %), and particle sizes (i.e., 100 μm, 1 mm, 1 cm). The resulting multiphase flow dynamics seem to be more sensitive to the geometric configuration than to the differences in initial and boundary conditions. As expected, the no-exit geometry (simulation A) initially generates the highest dynamic pressure ($\sim 10^6$ Pa) because no granular material can leave the system and, therefore, the mixture density can only increase with time. However, as more granular material is brought up into the drift, this scenario eventually leads to the formation of a granular deposit: namely, at the end of the drift, after 1 min there is little flow dynamics but an idle deposit. The more likely, one-exit geometry (simulation B) leads to the smallest dynamic pressures (100 to 10^5 maximum Pa). This is mostly due to a competition between the down drift (from the inlet) and return (toward the inlet) granular flows which create highly complex and chaotic dynamic patterns where these two flows meet. Hence, these circulating flows dynamically tend to counteract each other, resulting in low horizontal speeds and, therefore, low dynamic pressures. The two-exit geometry (simulation C) exhibits intermediate behavior with a down-drift multiphase flow on the roof and a return flow on the floor. The whole system forms a clearly defined recirculating pattern in the drift with some materials leaving the system and some recycling back into the drift along the roof. This highly dynamic scenario leads to relatively high dynamic pressures ($\sim 10^4$ to 10^5 Pa). Although the flow dynamics in the drifts are mostly controlled by the geometric configuration, the water vapor content in the dike is also important. A more dilute flow (4.6 wt %) is able to maintain a slow flow on the roof of the drift and a more turbulent gas-particle mixture over the whole height of the drift; hence it generates higher dynamic pressures.

[60] We have also explored the emptying scenario of a pressurized and previously pyroclast-filled drift. We used the same boundary and initial conditions as used by *Dartevelle and Valentine* [2005], except that we modeled larger particles (1 mm instead of 100 μm). The dynamics are essentially the same as by *Dartevelle and Valentine* [2005]: the drift empties itself from the top to bottom but only partially. Indeed, the initial pressure difference between the dike opening and the drift creates a drift wind strong enough to remove the particles at the top of the drift with a rarefaction ("emptying") wave moving down drift. Eventually, as the remaining particles settle down and pressure in the drift decreases to an atmospheric pressure, an idle granular deposit forms with a thickness of ~ 1.5 m.

[61] The work reported here is part of a larger effort to support probabilistic risk assessment for the proposed Yucca Mountain radioactive waste repository. As summarized by *Valentine* [2005] and *Valentine and Perry* [2009], risk assessment involves developing an understanding of the underlying processes that might accompany a volcanic
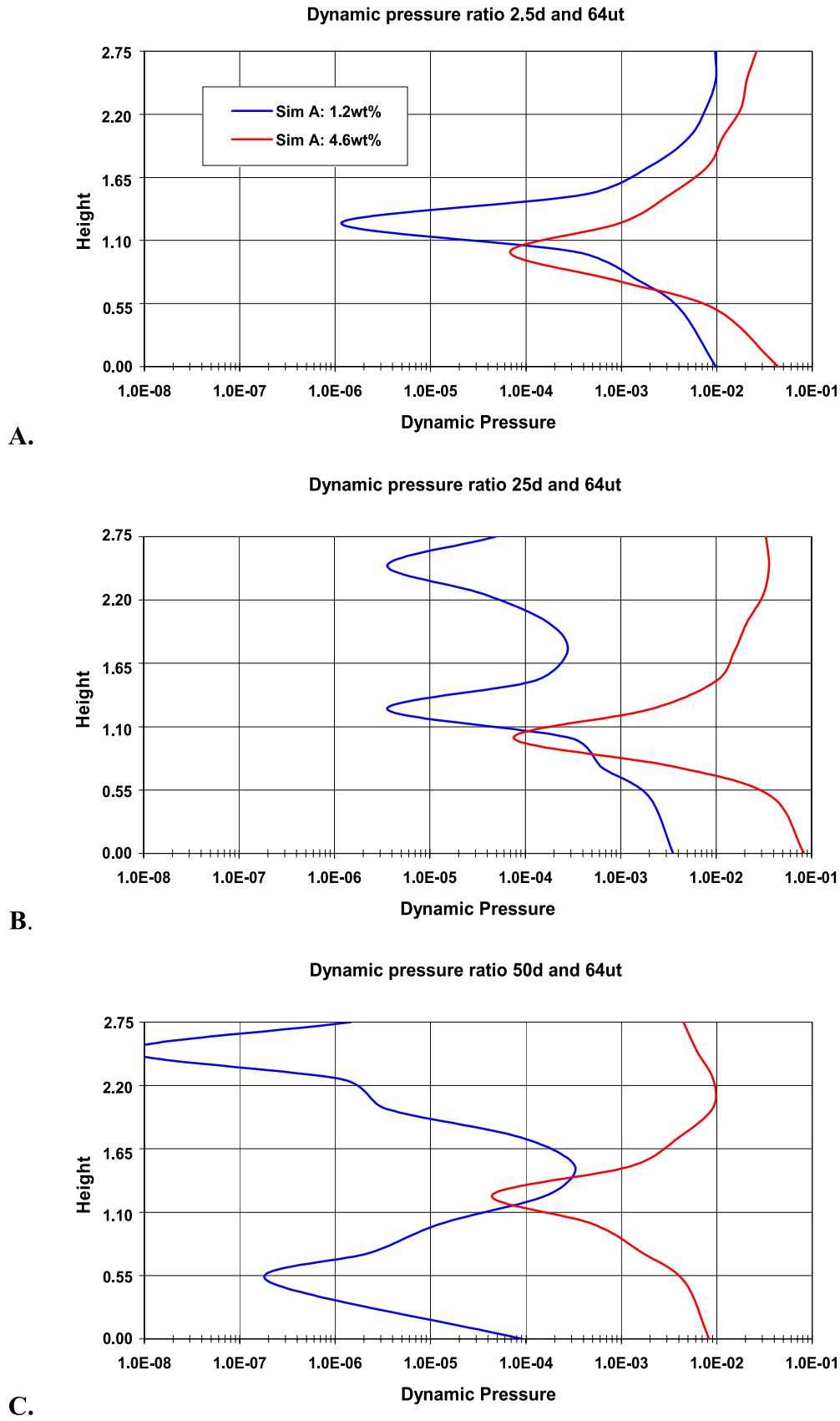
Dynamic pressure ratio 2.5d and 64ut

A.

Dynamic pressure ratio 25d and 64ut

B.

Dynamic pressure ratio 50d and 64ut

C.

Figure 15. Dimensionless dynamic pressures for simulation A (no exit) sampled at a distance of (a) 2.5d, (b) 25d, and (c) 50d and at time 64ut. All axes are dimensionless; d is a dimensionless unit of length (the inlet width), and ut is a dimensionless unit of time.
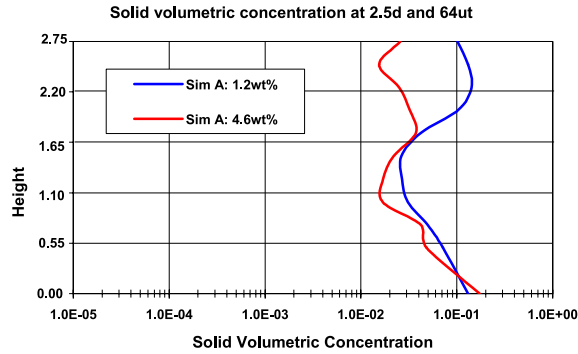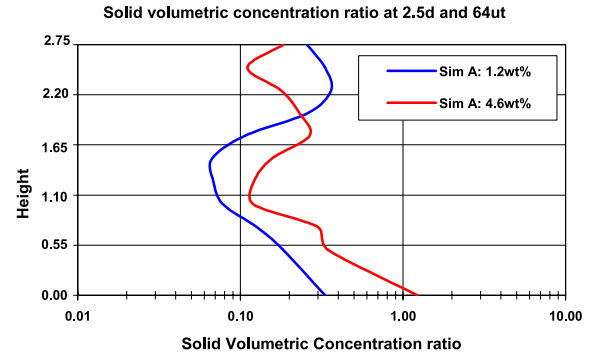
Dynamic pressure at 50 m and 10.5 s

A.

Dynamic pressure at 50 m and 60 s
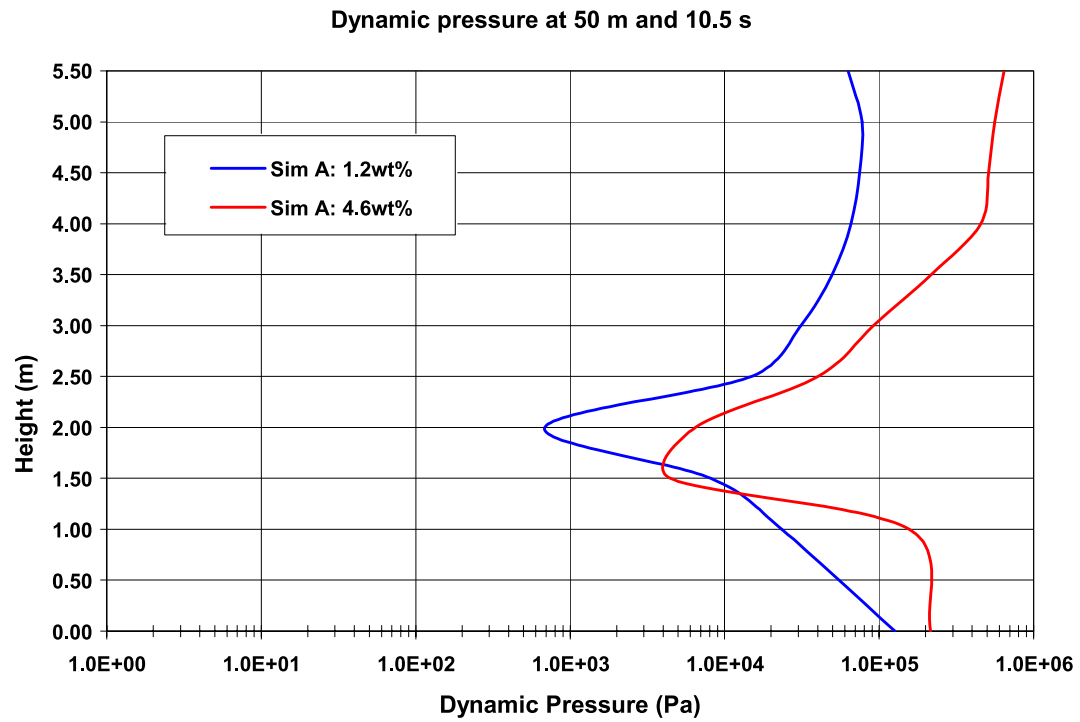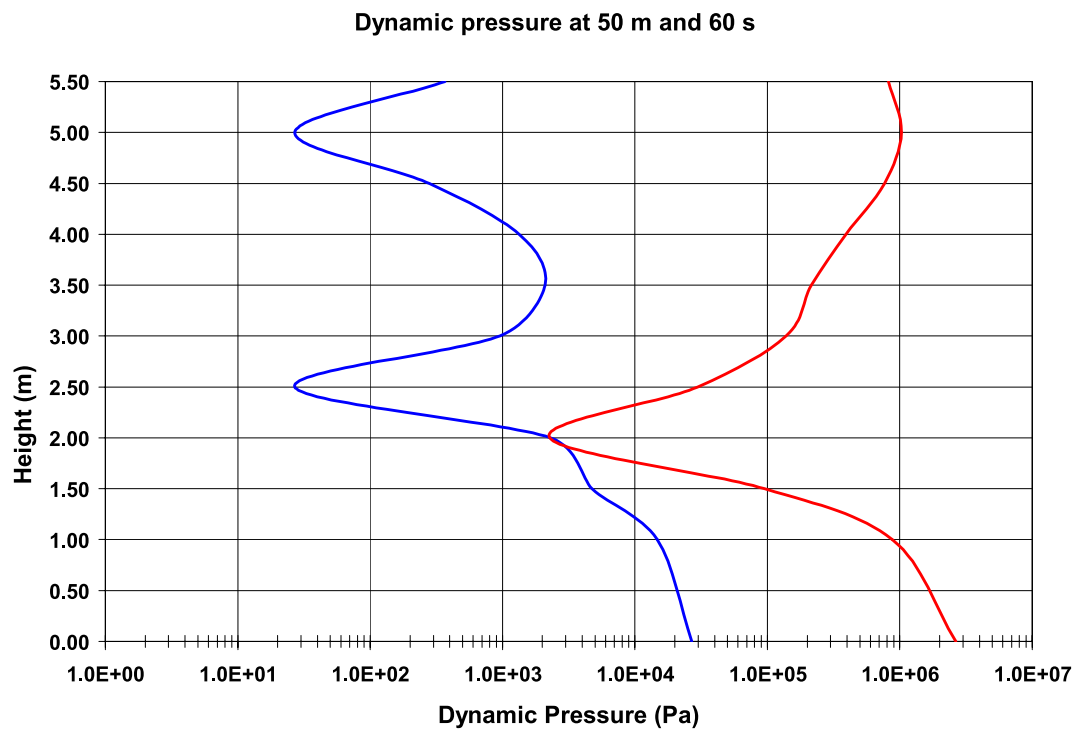
B.

Figure 16. Dynamic pressures for simulation A (no exit) sampled at 50 m, at times (a) 10.5 s and (b) 60 s. Vertical axis is in m; horizontal axis is in Pa (log scale).

A.

B.

C.
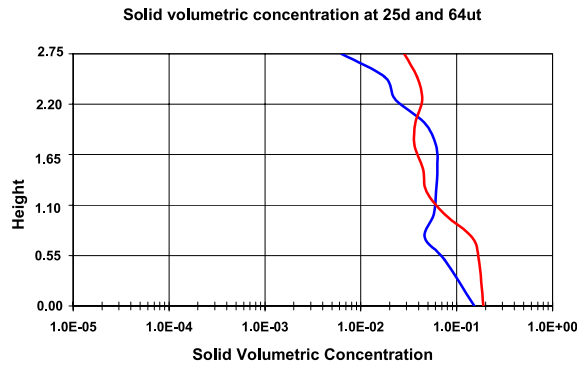
D.
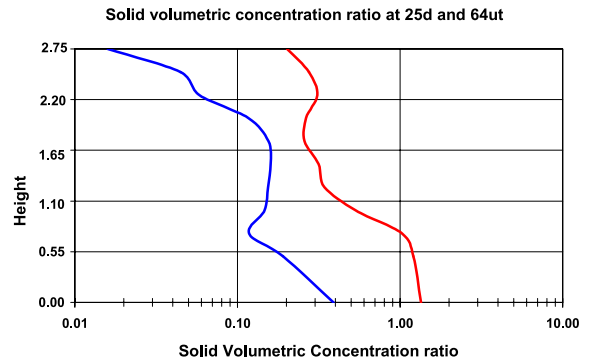
E.
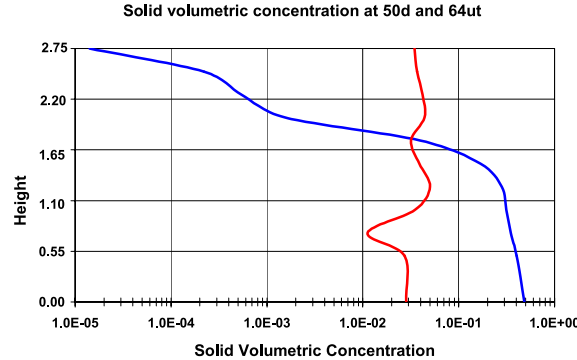
F.
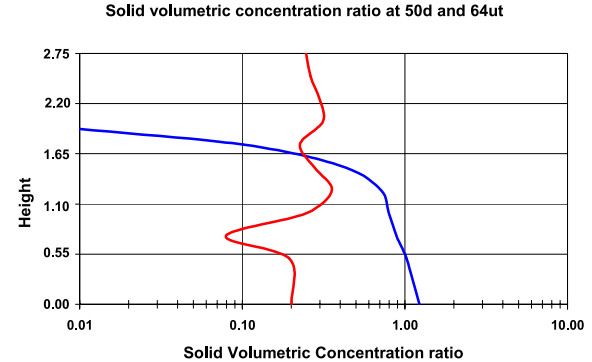
Figure 17. (left) Solid volumetric concentrations and (right) ratio of solid volumetric concentration (normalized by the concentration at the inlet) for simulation A (no exit) sampled at a distance of (a, b) 2.5d, (c, d) 25d, and (e, f) 50d. All axes are dimensionless; d is a dimensionless unit of length which has been normalized by the reference length scale (the inlet width), and ut is a dimensionless unit of time defined from the mixture vertical speed. Note that for the Lwv flow (blue curve), in Figure 17e, the formation of a granular deposit (in this case, the granular concentration is increasing with respect to the inlet concentration; see Figure 17f).

event, and using that understanding to develop simplified probabilistic models that account for the range of parameter values and uncertainties that are inherent in predicting such an event. Our results on the range of flow conditions within drifts can be used in turn by engineers to assess the response of waste packages and other repository components; those predictions also have wide ranges of parameter combinations and uncertainties that are accounted for by simplified probabilistic response models. All of the simplified models are then integrated in a manner that gives a final, relatively straightforward result. In the case of Yucca Mountain risk assessment, that result is simply the expected range of radiation dose to a defined population, weighted by the probability of a volcanic event. The current approach for volcanic risk assessment at Yucca Mountain assumes, at the simplified model level, that all waste packages in the repository are compromised in terms of their ability to act as barriers to radionuclide migration if a dike hits any drift.

A.

Solid volumetric concentration at 50 m and 10.5 s

B.

Solid volumetric concentration ratio at 50 m and 10.5s

C.

Solid volumetric concentration at 50 m and 60 s

D.

Solid volumetric concentration ratio at 50 m and 60 s
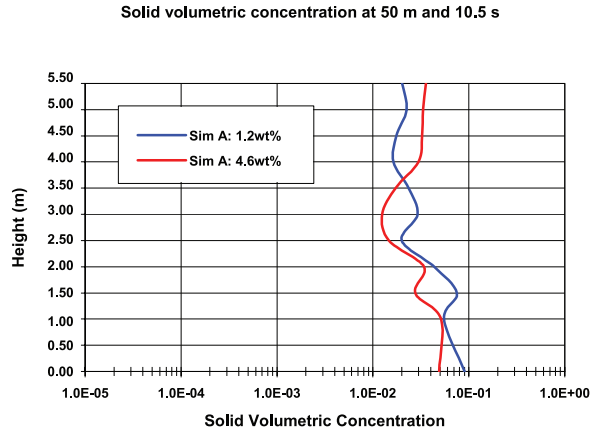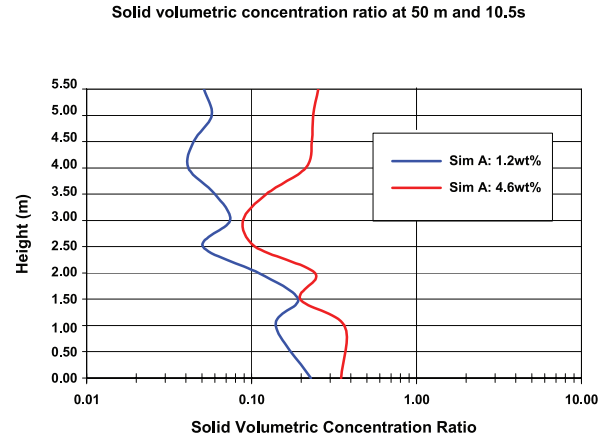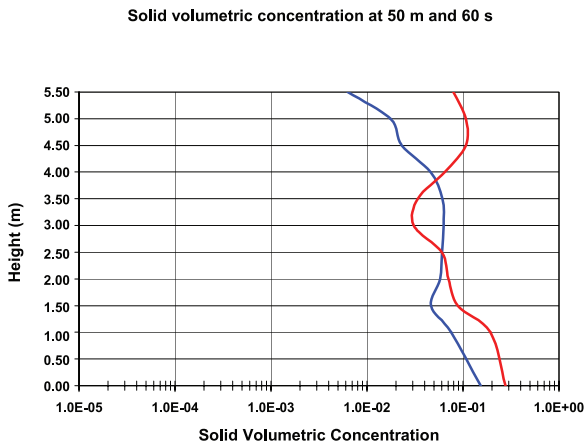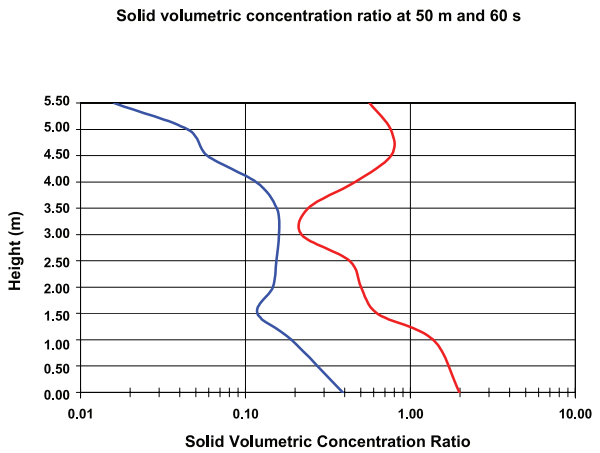
Figure 18. (left) Solid volumetric concentrations and (right) ratio of solid volumetric concentration (normalized by the concentration at the inlet) for simulation A (no exit) sampled at 50 m at times (a, b) 10.5 s and (c, d) 60 s. Vertical axis is in m; horizontal axis is dimensionless (log scale).

As a result, any seepage waters that encounter a basalt-filled drift are assumed to dissolve radionuclides and potentially transport them downward to the water table. Furthermore, any waste packages that are intersected by an eruptive conduit are assumed to break down and allow the mechanical transport of radionuclides such that they erupt onto the surface. Some of that contaminated ejecta may be dispersed downwind to become a component of radioactive dose.

9. Conclusion

[62] We have applied the multiphase hydrodynamics code GMFIX (version 1.62) to understand the range of processes that might occur if a pyroclastic particle-gas mixture were to intersect repository openings at Yucca Mountain. Simulations indicate that the particle-gas mixtures expand and flow down horizontal drifts in complex ways and with some component of counterflow toward the feeder dike. Scenarios where a dike-drift system is already filled with pressurized gas and pyroclasts that is subsequently allowed to decompress indicate that much of the return flow from a drift to the feeder dike occurs along the roof of the drift. The processes

are sensitive to the geometry of the interaction, to particle size (i.e., degree of fragmentation), and to volatile content, and are likely also sensitive to mass fluxes and pressure boundary conditions.

[63] The work reported here contributes to our overall understanding of the types of processes that might occur if the plumbing of a new monogenetic volcano were to intersect the potential repository. This information can be used by engineers to assess the impacts of the range of simulated conditions on waste packages and other components of the repository system. In this manner, our work supports the development and testing of more simplified models, which account for the wide ranges of parameter combinations and uncertainties, that are used in a probabilistic risk assessment. Although our focus has been on the rather unique subsurface facility that might be constructed at Yucca Mountain, the same approach can be used for more typical volcanic risk assessment studies such as those involving large urban areas. It is important to bear in mind that complex fluid and solid mechanics models, and the numerical and laboratory experiments that are used to
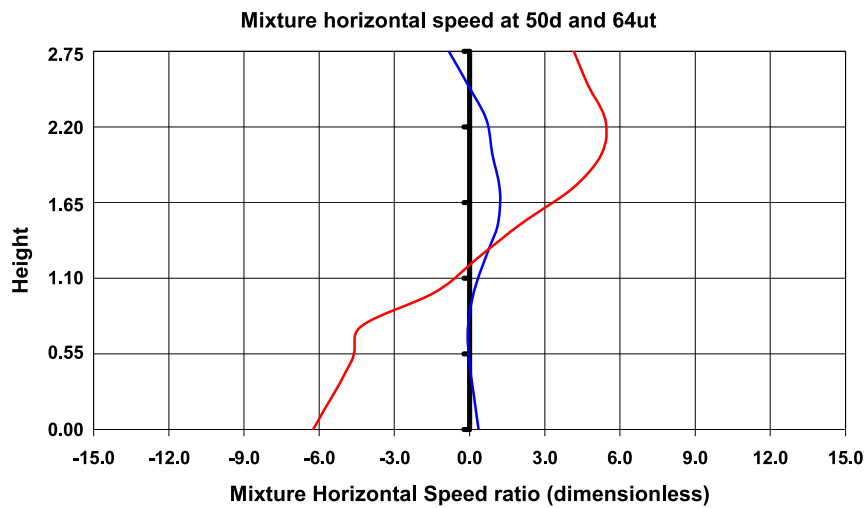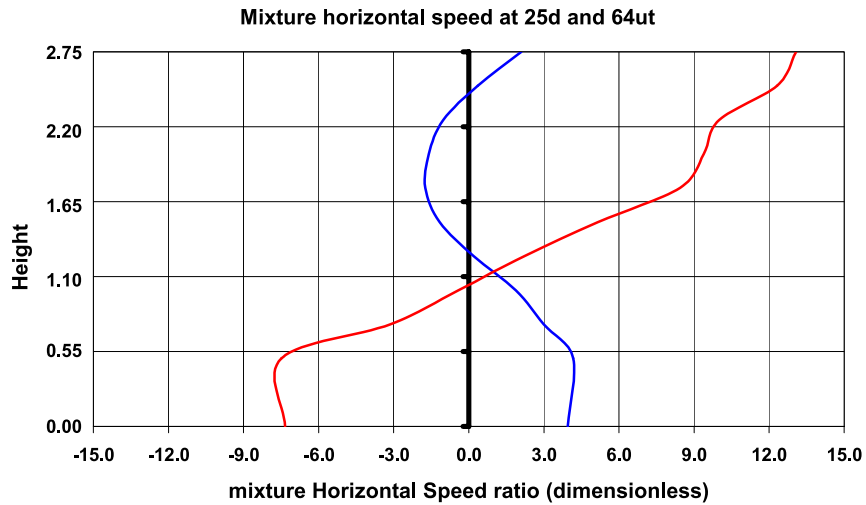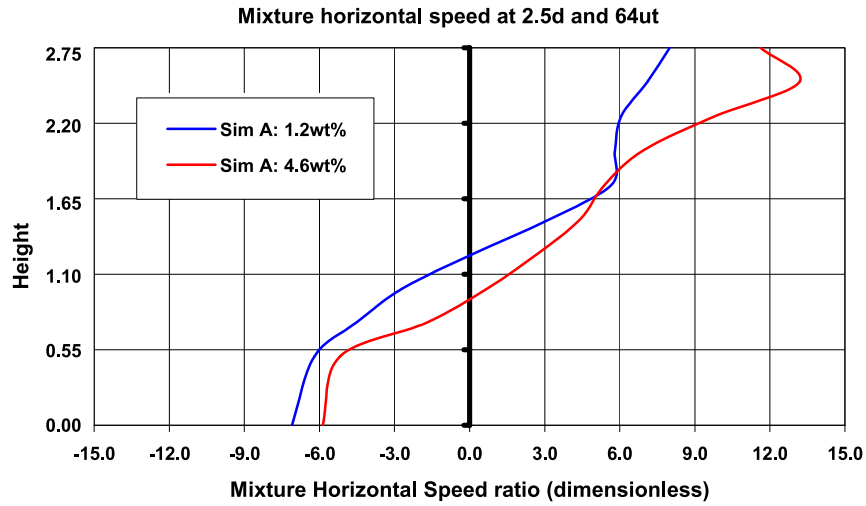
Mixture horizontal speed at 2.5d and 64ut

A.

Mixture horizontal speed at 25d and 64ut

B.

Mixture horizontal speed at 50d and 64ut

C.

Figure 19.   Dimensionless mixture horizontal speed for simulation A (no exit) sampled at a distance of (a) 2.5d, (b) 25d, and (c) 50d and at 64 ut. All axes are dimensionless; d is a dimensionless unit of length (normalized by the inlet width), and ut is a dimensionless unit of time. Note the quasi-idle speed for the Lwv flow (blue curve in Figure 19c), which indicates when compared with Figure 17e, the formation of a granular deposit.

Table 9. Gas Density Sampled at 10.5 s for Simulation A (No-Exit Geometry)

Water Vapor Mass Fraction (wt %)	Averaged Gas Density (kg/m³)	
	10 m Down Drift, 10.5 s	150 m Down Drift, 10.5 s
1.2 (Lwv)	0.85	2.16
4.6 (Hwv)	1.14	1.48

understand them, do not provide "final" answers for risk assessment studies, but must be used to support the development of simplified probabilistic models that account for a wide range of processes and parameter uncertainties and that produce a relatively straightforward, probabilistic risk assessment result.

A.

Solid volumetric concentration at 10 m and 18.25 s

B.

Dynamic pressure at 10 m and 18.25 s

C.

Solid volumetric concentration at 10 m and 18.25 s

D.

Dynamic pressure at 10 m and 18.25 s

E.

Solid volumetric concentration at 10 m and 18.25 s

F.

Dynamic pressure at 10 m and 18.25 s
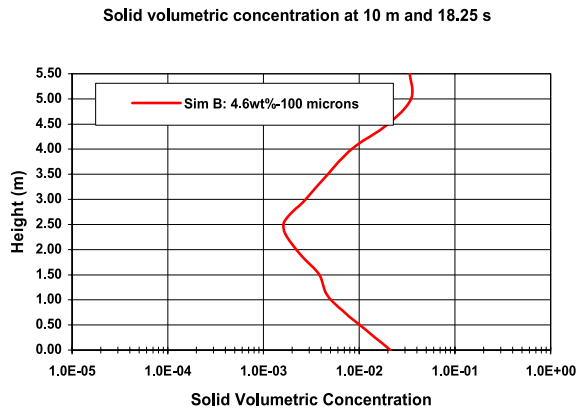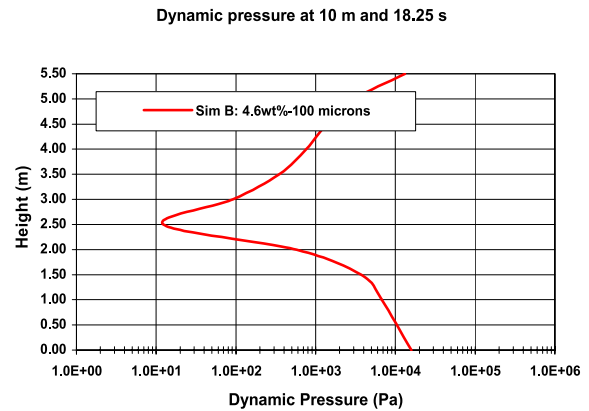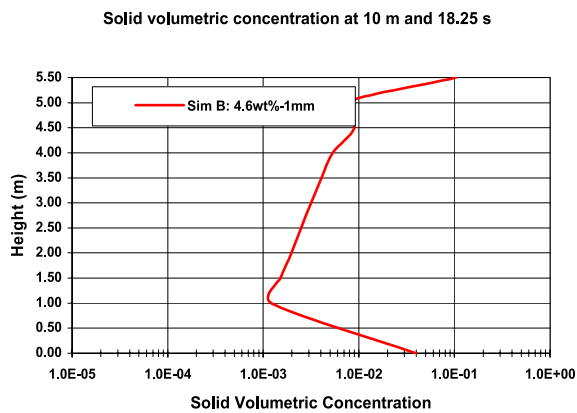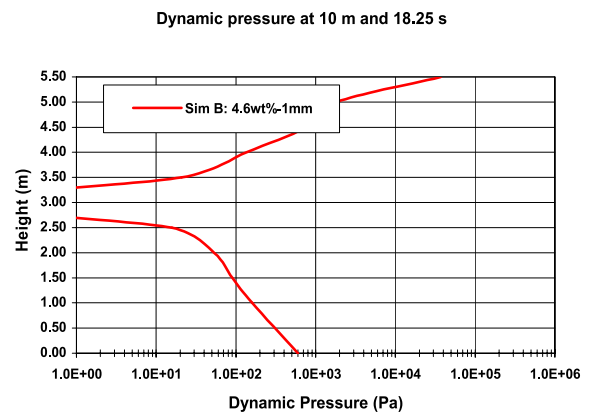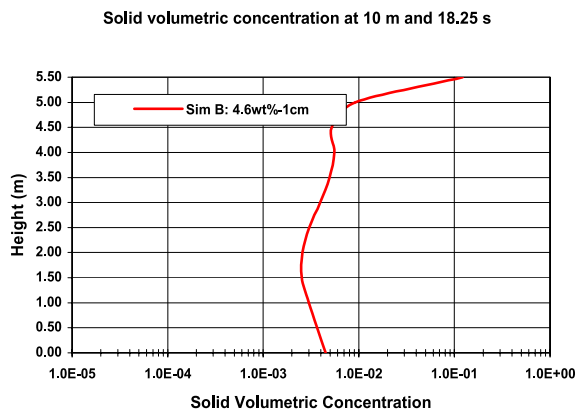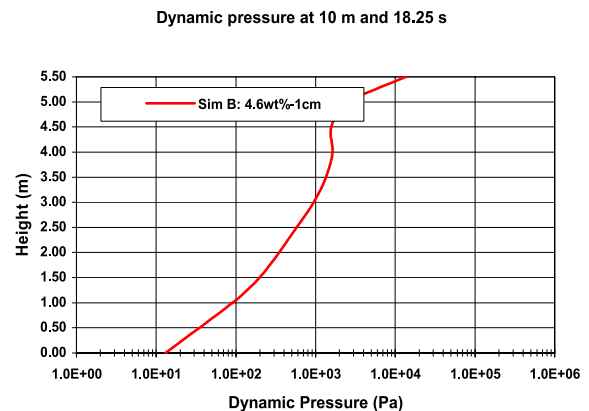
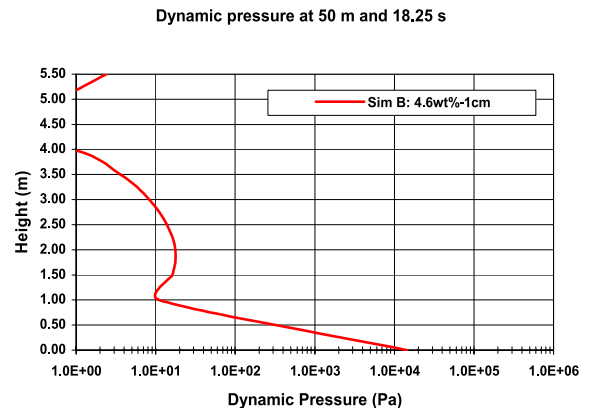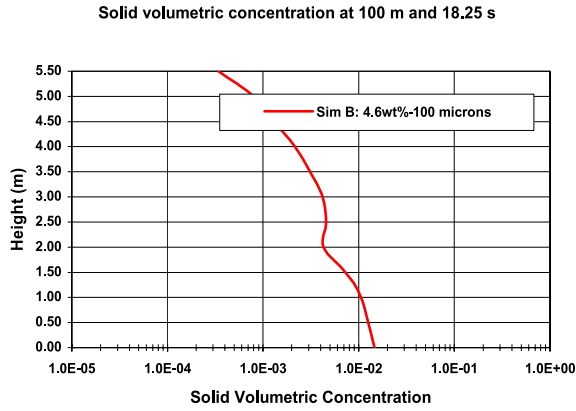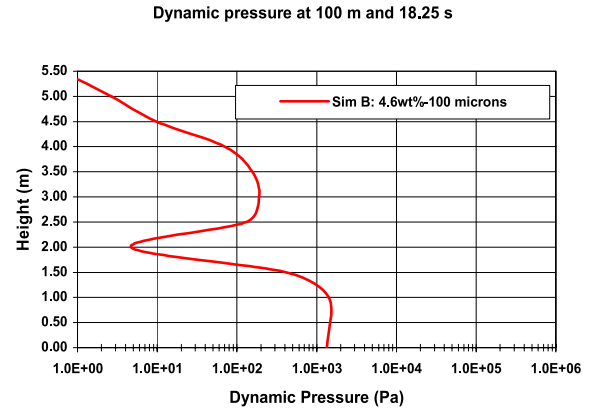**Figure 20.** (left) Solid volumetric concentrations and (right) dynamic pressure (in Pa) sampled at 18.25 s and 10 m down the drift for geometry B (one exit to the surface) and a 4.6 wt % water vapor enriched flow at the inlet. (a, b) For the 100 μm diameter particles, (c, d) for the 1 mm diameter particles, and (e, f) for the 1 cm diameter particles case.

A.
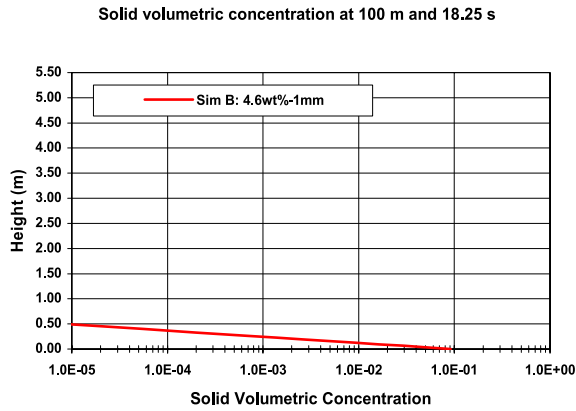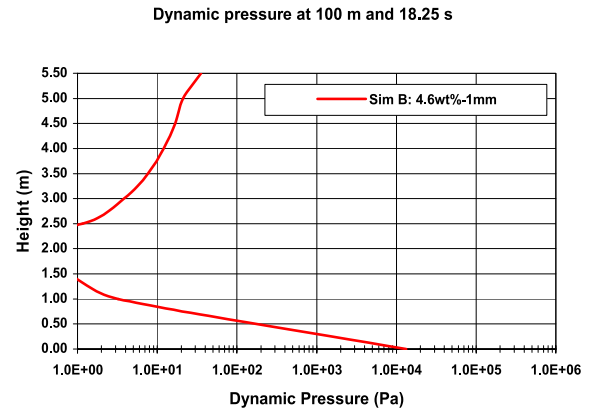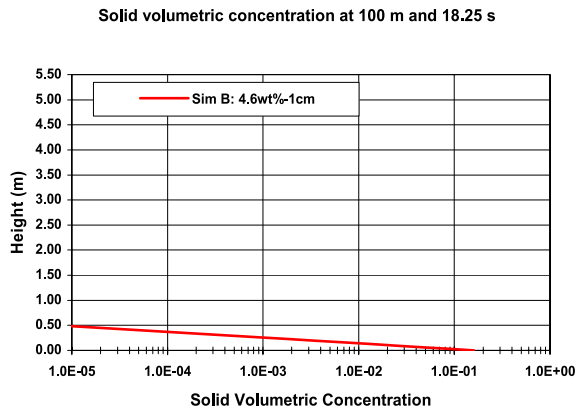
Solid volumetric concentration at 50 m and 18.25 s

B.

Dynamic pressure at 50 m and 18.25 s

C.

Solid volumetric concentration at 50 m and 18.25 s

D.

Dynamic pressure at 50 m and 18.25 s

E.

Solid volumetric concentration at 50 m and 18.25 s

F.

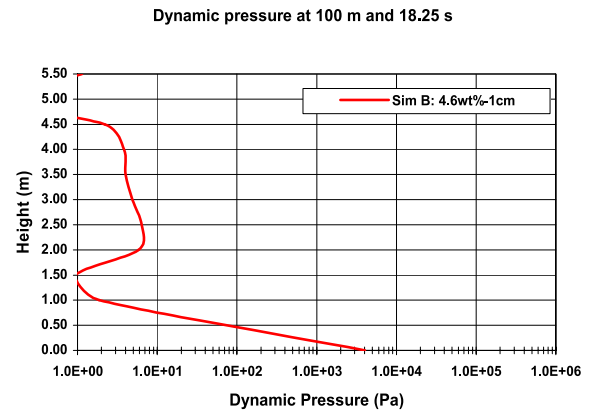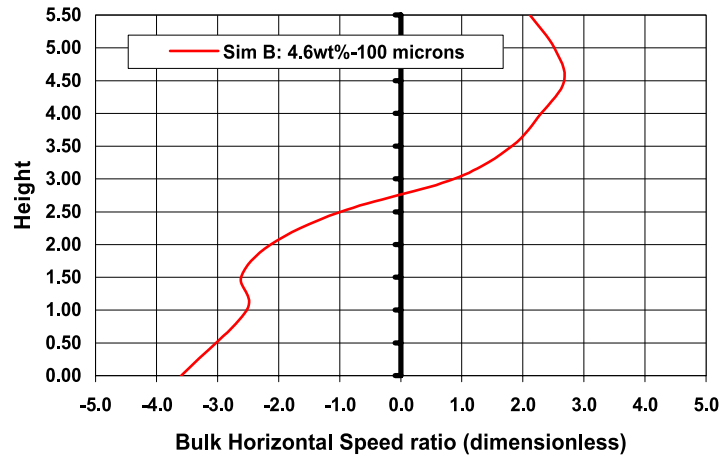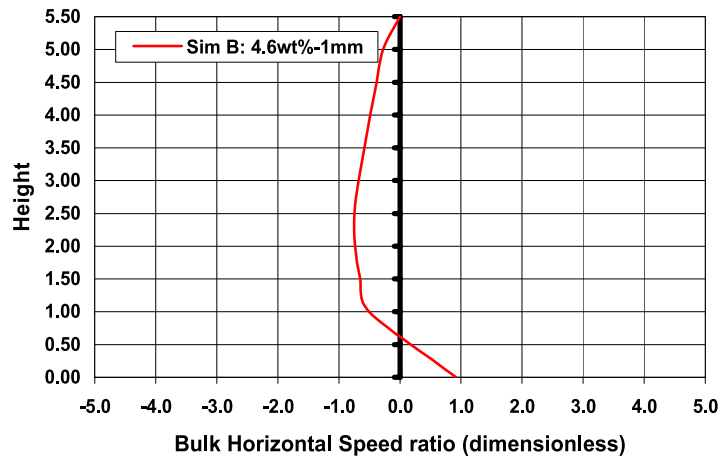Dynamic pressure at 50 m and 18.25 s
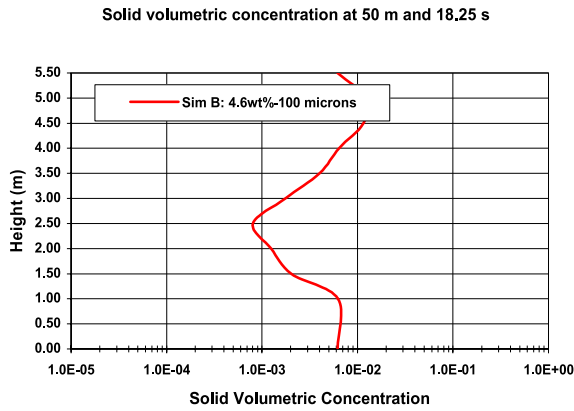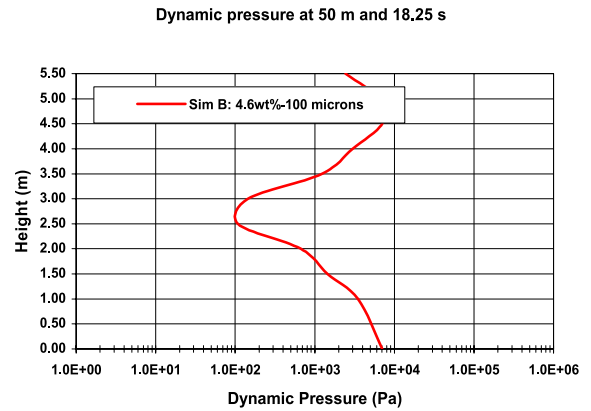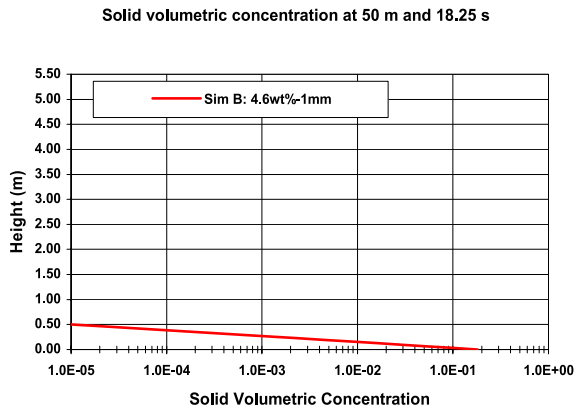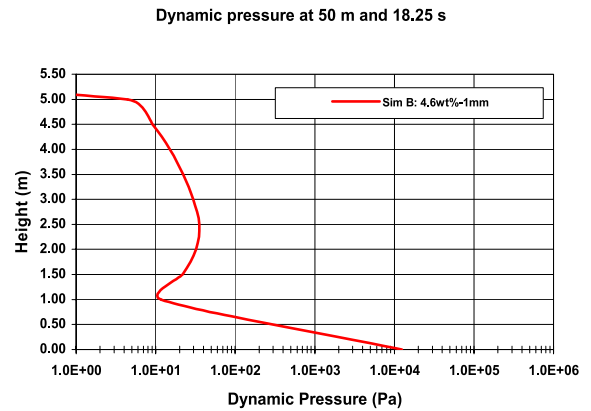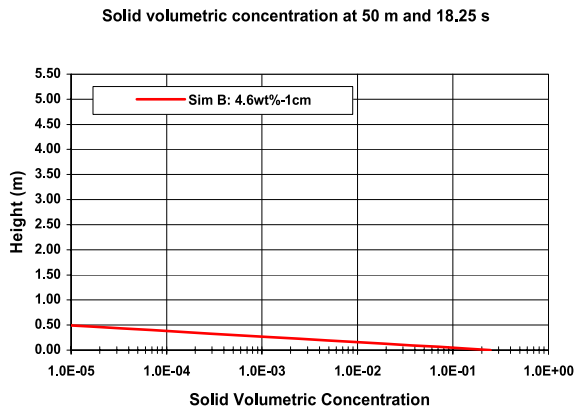
Figure 21. (left) Solid volumetric concentrations and (right) dynamic pressure (in Pa) sampled at 18.25 s and 50 m down in the drift tunnel for the geometry B (one exit to the surface) and a 4.6 wt % water vapor enriched flow. (a, b) For the 100 μm diameter particles, (c, d) for the 1 mm diameter particles, and (e, f) for the 1 cm diameter particles case.

A.

Solid volumetric concentration at 100 m and 18.25 s

B.

Dynamic pressure at 100 m and 18.25 s

C.

Solid volumetric concentration at 100 m and 18.25 s

D.

Dynamic pressure at 100 m and 18.25 s

E.

Solid volumetric concentration at 100 m and 18.25 s

F.

Dynamic pressure at 100 m and 18.25 s

Figure 22. (left) Solid volumetric concentrations and (right) dynamic pressure (in Pa) sampled at 18.25 s and 100 m down in the drift tunnel for the geometry B (one exit to the surface) and a 4.6 wt % water vapor enriched flow. (a, b) For the 100 μm diameter particles, (c, d) for the 1 mm diameter particles, and (e, f) for the 1 cm diameter particles case.

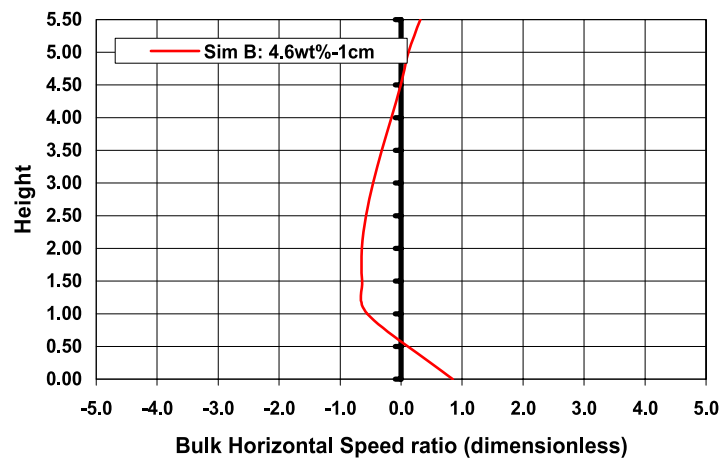**Mixture horizontal speed ratio at 50 m and 18.5 s**

Sim B: 4.6wt%-100 microns

Bulk Horizontal Speed ratio (dimensionless)

A.

Mixture horizontal speed ratio at 50 m and 18.5 s

Sim B: 4.6wt%-1mm

Bulk Horizontal Speed ratio (dimensionless)

B.

Mixture horizontal speed ratio upon at 50 m and 18.5 s

Sim B: 4.6wt%-1cm

Bulk Horizontal Speed ratio (dimensionless)

C.

Figure 23. Dimensionless mixture horizontal speed for simulation B (one exit) sampled at a distance of 50 m in the drift tunnel at 18.25 s for the (a) 100 μm, (b) 1 mm, and (c) 1 cm diameter particles. Notice that the least inertial particles (100 μm) develop the most sheared and fastest flow as well as the most turbulent and diluted flows (compare with Figure 19).
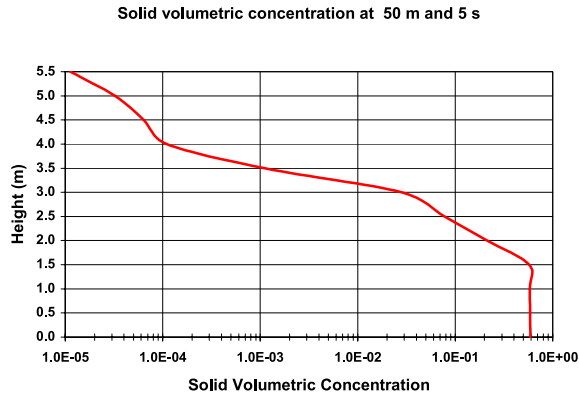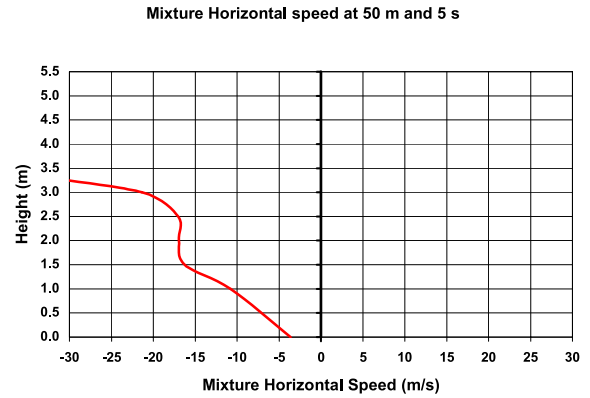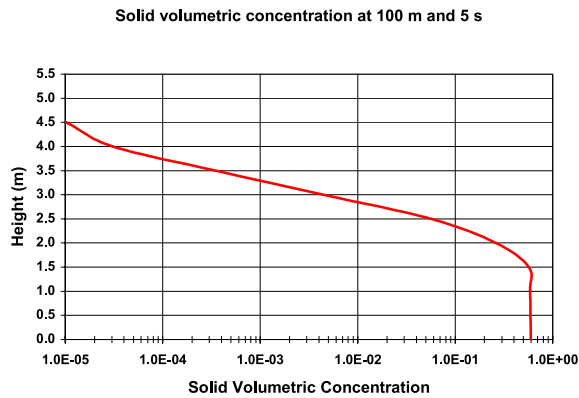
A.

Solid volumetric concentration at 10 m and 5 s

B.

Mixture Horizontal speed at 10 m and 5 s

C.

Solid volumetric concentration at 50 m and 5 s

D.

Mixture Horizontal speed at 50 m and 5 s

E.

Solid volumetric concentration at 100 m and 5 s

F.

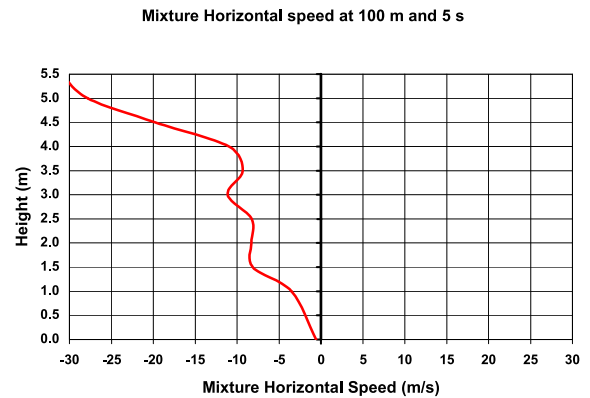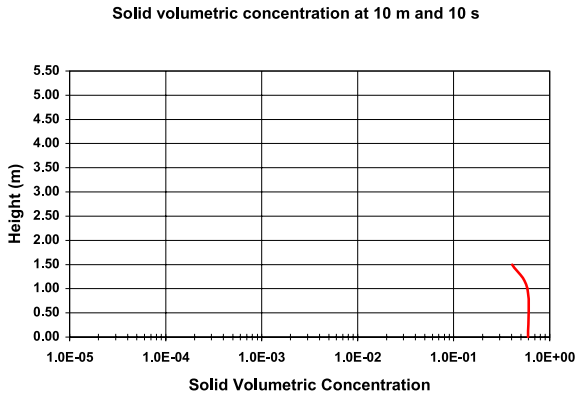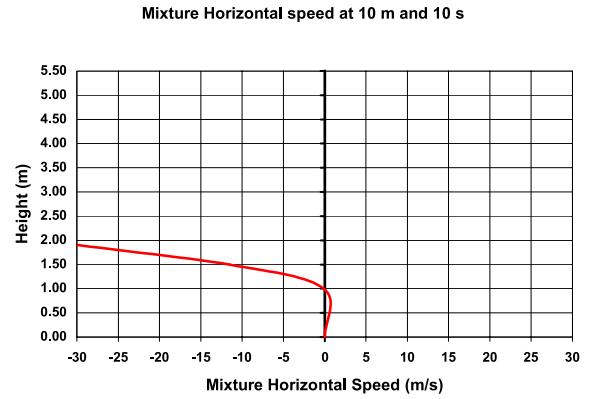Mixture Horizontal speed at 100 m and 5 s
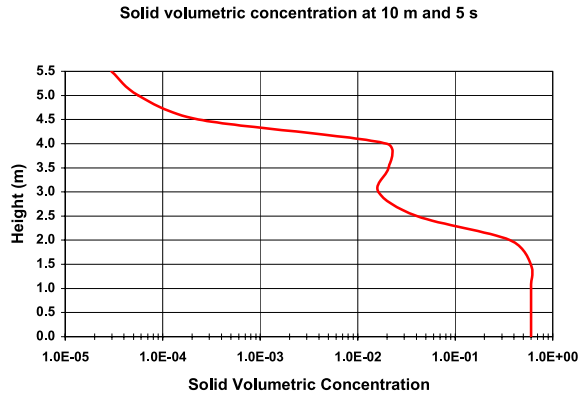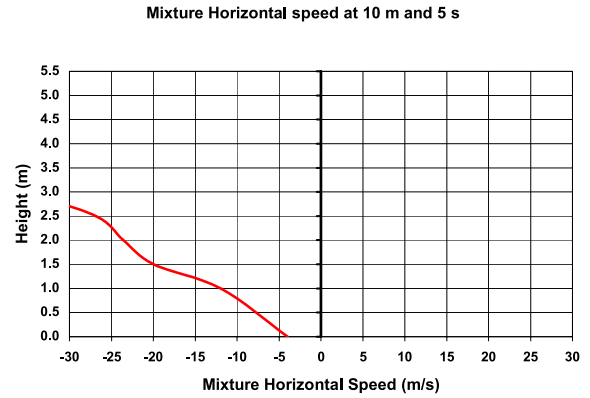
Figure 24. (left) Volumetric solid concentration and (right) mixture horizontal speed sampled 5 s after a sudden opening of a drift tunnel initially filled with pyroclastic materials. (a, b) Sampled 10 m away from the opening, (c, d) sampled 50 m in the tunnel, and (e, f) sampled 100 m in the drift tunnel. Notice that the highest horizontal speeds are at the top of the drift tunnel; the system is being emptied from top to bottom.
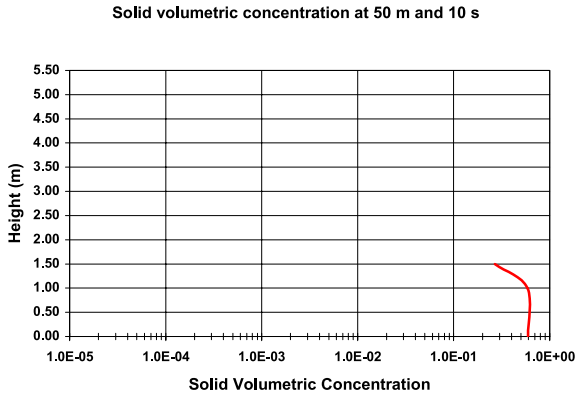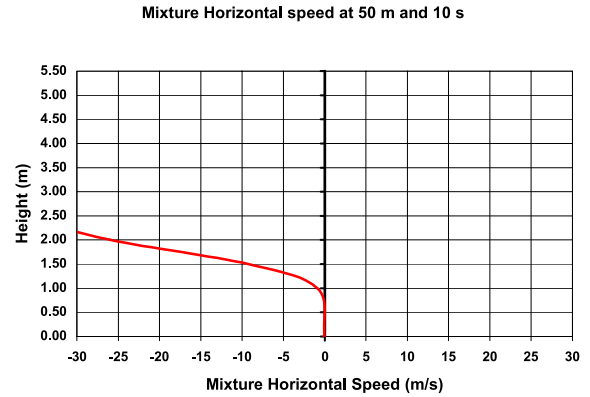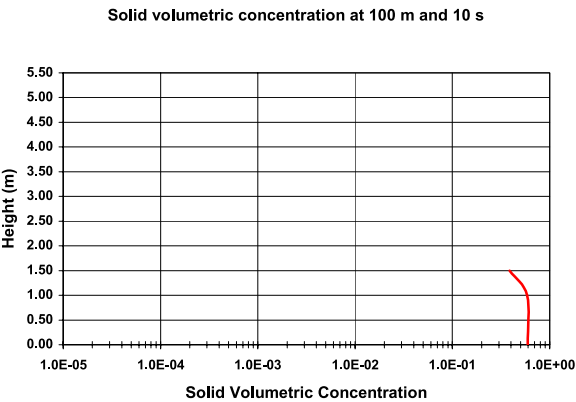
A.

Solid volumetric concentration at 10 m and 10 s

B.

Mixture Horizontal speed at 10 m and 10 s

C.

Solid volumetric concentration at 50 m and 10 s

D.

Mixture Horizontal speed at 50 m and 10 s

E.

Solid volumetric concentration at 100 m and 10 s

F.

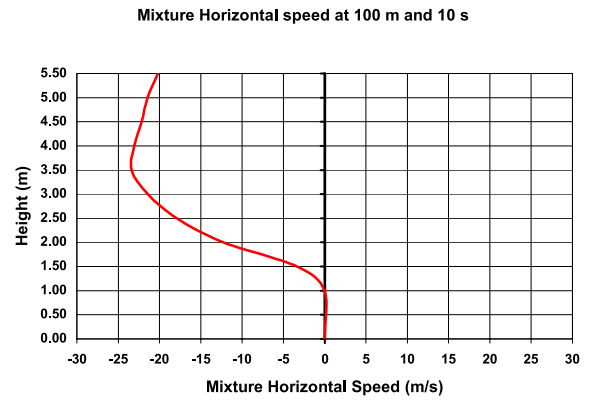Mixture Horizontal speed at 100 m and 10 s

Figure 25. (left) Volumetric solid concentration and (right) mixture horizontal speed sampled 10 s after a sudden opening of a drift tunnel initially filled with pyroclastic materials. (a, b) Sampled 10 m away from the opening, (c, d) sampled 50 m in the tunnel, and (e, f) sampled 100 m in the drift tunnel. Notice that the remaining granular material is quasi at rest (~zero horizontal speed) and formed a granular deposit. In 10 s, only the top part of the drift tunnel (over 4 m) has been emptied.

References

Benyahia, S., M. Syamlal, and T. J. O'Brien (2005), Evaluation of boundary conditions used to model dilute turbulent gas/solid flows in a pipe, *Powder Technol.*, 156, 62–72, doi:10.1016/j.powtec.2005.04.002.

Bradshaw, T. K., and H. E. I. Smith (1994), Polygenetic Quaternary volcanism at Crater Flat, Nevada, *J. Volcanol. Geotherm. Res.*, 63, 165–182, doi:10.1016/0377-0273(94)90072-8.

Bechtel SAIC Company (BSC) (2004a), Characterize framework for igneous activity at Yucca Mountain, Nevada, *Rep. ANL-MGR-GS-000001 REV 02*, Las Vegas, Nev.

Bechtel SAIC Company (BSC) (2004b), Dike/drift interactions, *Rep. MDL-MGR-GS-000005 REV 01*, Las Vegas, Nev.

Connor, C. B., and B. E. Hill (1995), Three nonhomogeneous Poisson models for the probability of basaltic volcanism: Application to the Yucca Mountain region, Nevada, *J. Geophys. Res.*, 100, 10,107–10,125, doi:10.1029/95JB01055.

Connor, C. B., J. A. Stamatakos, D. A. Ferrill, B. E. Hill, G. I. Ofoegbu, F. M. Conway, B. Sagar, and J. Trapp (2000), Geologic factors controlling patterns of small-volume basaltic volcanism: Application to a volcanic hazards assessment at Yucca Mountain, Nevada, *J. Geophys. Res.*, 105, 417–432, doi:10.1029/1999JB900353.

Crowe, B. M. (1986), Volcanic hazard assessment for disposal of highlevel radioactive waste, in *Active Tectonics*, pp. 247–260, Natl. Acad. Press, Washington, D. C.

Crowe, B. M., M. E. Johnson, and R. J. Beckman (1982), Calculation of the probability of volcanic disruption of a high-level radioactive waste repository within southern Nevada, USA, *Radioact. Waste Manage. Nucl. Fuel Cycle*, 3, 167–190.

Dartevelle, S. (2004), Numerical modeling of geophysical granular flows: 1. A comprehensive approach to granular rheologies and geophysical multiphase flows, *Geochem. Geophys. Geosyst.*, 5, Q08003, doi:10.1029/2003GC000636.

Dartevelle, S. (2005), Comprehensive approaches to multiphase flows in geophysics: Application to non-isothermal, non-homogenous, unsteady, large-scale, turbulent dusty clouds. I. Basic RANS and LES Navier-Stokes equations, *LA-14228*, 51 pp., Los Alamos Natl. Lab., Los Alamos, N. M.

Dartevelle, S. (2006a), Software validation report for GMFIX v. 1.62, *Rep. 11192-SVR-1.62–00-WinXP*, U.S. Dep. of Energy, Off. of Reposit. Dev., Las Vegas, Nev.

Dartevelle, S. (2006b), User information document for GMFIX v. 1.62, *Rep. 11192-UID-1.62–00*, U.S. Dep. of Energy, Off. of Reposit. Dev., Las Vegas, Nev.

Dartevelle, S. (2006c), Design document for GMFIX v. 1.62, *Rep. 11192-DD-1.62–00*, U.S. Dep. of Reposit. Dev., Las Vegas, Nev.

Dartevelle, S. (2007), From model conception to verification and validation. A global approach to multiphase Navier-Stoke models with an emphasis to volcanic explosive phenomenology, *Rep. LA-14346*, Los Alamos Natl. Lab., Los Alamos, N. M.

Dartevelle, S., and G. A. Valentine (2005), Early time multiphase interactions between basaltic magma and underground repository openings at the proposed Yucca Mountain radioactive waste repository, *Geophys. Res. Lett.*, 32, L22311, doi:10.1029/2005GL024172.

Dartevelle, S., and G. A. Valentine (2007a), Transient multiphase processes during the explosive eruption of basalt through a geothermal borehole (Námafjall, Iceland, 1977) and implications for natural volcanic flows, *Earth Planet. Sci. Lett.*, 262, 363–384, doi:10.1016/j.epsl.2007.07.053.

Dartevelle, S., and G. A. Valentine (2007b), Interaction of multiphase magmatic flows with underground openings at the proposed Yucca Mountain radioactive waste repository (southern Nevada, USA), *Rep. LA-UR-07–3579*, 53 pp., Los Alamos Natl. Lab., Los Alamos, N. M.

Dartevelle, S., W. I. Rose, J. Stix, K. Kelfoun, and J. W. Vallance (2004), Numerical modeling of geophysical granular flows: 2. Computer simulations of Plinian clouds and pyroclastic flows and surges, *Geochem. Geophys. Geosyst.*, 5, Q08004, doi:10.1029/2003GC000637.

Fleck, R. J., B. D. Turrin, D. A. Sawyer, R. G. Warren, D. E. Champion, M. R. Hudson, and S. A. Minor (1996), Age and character of basaltic rocks of the Yucca Mountain region, southern Nevada, *J. Geophys. Res.*, 101, 8205–8227, doi:10.1029/95JB03123.

Heizler, M. T., F. V. Perry, B. M. Crowe, L. Peters, and R. Appelt (1999), The age of the Lathrop Wells volcanic center: An ^{40}Ar/^{39}Ar dating investigation, *J. Geophys. Res.*, 104, 767–804, doi:10.1029/1998JB900002.

Hishida, K., K. Takemoto, and M. Maeda (1987), Turbulence characteristics of gas-solids two-phase confined jet (effect of particle density), *Jpn. J. Multiphase Flow*, 1, 56–68.

Keating, G. N., G. A. Valentine, D. J. Krier, and F. V. Perry (2008), Shallow plumbing systems for small volume basaltic volcanoes, *Bull. Volcanol.*, 70, 563–582, doi:10.1007/s00445-007-0154-1.

Ladenburg, R., C. C. van Voorhis, and J. Winckler (1949), Interferometric studies of faster than sound phenomena. Part II. Analysis of supersonic air jets, *Phys. Rev.*, 76, 662–677, doi:10.1103/PhysRev.76.662.

Larsen, G., K. Gronvold, and S. Thorarinson (1979), Volcanic eruption through a geothermal borehole at Namafjall, Iceland, *Nature*, 278, 707–710, doi:10.1038/278707a0.

Lewis, C. H., Jr., and D. J. Carlson (1964), Normal shock location in underexpanded gas and gas-particle jets, *AIAA J.*, 2, 776–777, doi:10.2514/3.2409.

Menand, T., and J. C. Phillips (2007), Gas segregation in dykes and sills, *J. Volcanol. Geotherm. Res.*, 159, 393–408, doi:10.1016/j.jvolgeores.2006.08.003.

Menand, T., J. C. Phillips, and R. S. J. Sparks (2008), Circulation of bubbly magma and gas segregation within tunnels of the potential Yucca Mountain repository, *Bull. Volcanol.*, 70, 947–960, doi:10.1007/s00445-007-0179-5.

Nicholis, M. G., and M. J. Rutherford (2004), Experimental constraints on magma ascent rate for the Crater Flat volcanic zone hawaiite, *Geology*, 32, 489–492, doi:10.1130/G20324.1.

Perry, F. V., B. M. Crowe, G. A. Valentine, and L. M. Bowker (1998), Volcanism studies: Final report for the Yucca Mountain Project, *Rep. LA-13478-MS*, Los Alamos Natl. Lab., Los Alamos, N. M.

Perry, F. V., G. A. Valentine, A. H. Cogbill, G. N. Keating, E. S. Gaffney, and B. Damjanac (2006), Control of basaltic feeder dike orientation by fault capture near Yucca Mountain, USA, *Eos Trans. AGU*, 87(52), Fall Meet. Suppl., Abstract V11B-0572.

Rubin, A. M. (1995), Propagation of magma-filled cracks, *Annu. Rev. Earth Planet. Sci.*, 23, 287–336, doi:10.1146/annurev.ea.23.050195.001443.

Simonin, O. (1996), Continuum modeling of dispersed two-phase flows, in *Combustion and Turbulence in Two-Phase Flows*, Lect. Ser., vol. 2, pp. 1–47, Von Karman Inst. of Fluid Dyn., Brussels.

Sandia National Laboratories (SNL) (2007a), Characterize eruptive processes at Yucca Mountain, Nevada, *Rep. ANL-MGR-GS-000002 REV 03*, Sandia Natl. Lab., Albuquerque, N. M.

Sandia National Laboratories (SNL) (2007b), Total system performance assessment data input package for number of waste packages hit by igneous events, *Rep. TDR-TDIP-DE-000004 Rev 00*, Sandia Natl. Lab., Albuquerque, N. M.

Symlal, M. (1998), MFIX documentation. Numerical technique, *Rep. DOE/MC31346–5824, DE98002029*, 80 pp., U.S. Dep. of Energy, Washington, D. C.

Valentine, G. A. (1998a), Eruption column physics, in *From Magma to Tephra: Modeling Physical Processes of Explosive Volcanic Eruptions*, edited by A. Freundt and M. Rosi, pp. 91–138, Elsevier, Amsterdam, Netherlands.

Valentine, G. A. (1998b), Damage structures by pyroclastic flows and surges, inferred from nuclear weapons effects, *J. Volcanol. Geotherm. Res.*, 87, 117–140, doi:10.1016/S0377-0273(98)00094-8.

Valentine, G. A. (2005), Predicting risks in the earth sciences–volcanological examples, *Los Alamos Sci.*, 29, 56–69.

Valentine, G. A., and G. N. Keating (2007), Eruptive styles and inferences about plumbing systems at Hidden Cone and Little Black Peak scoria cone volcanoes (Nevada, U.S.A.), *Bull. Volcanol.*, 70, 105–113, doi:10.1007/s00445-007-0123-8.

Valentine, G. A., and K. E. C. Krogh (2006), Emplacement of shallow dikes and sills beneath a small basaltic volcanic center—The role of pre-existing structure (Paiute Ridge, southern Nevada, USA), *Earth Planet. Sci. Lett.*, 246, 217–230, doi:10.1016/j.epsl.2006.04.031.

Valentine, G. A., and F. V. Perry (2006), Decreasing magma tic footprints of individual volcanoes in a waning basaltic field, *Geophys. Res. Lett.*, 33, L14305, doi:10.1029/2006GL026743.

Valentine, G. A., and F. V. Perry (2007), Tectonically controlled, time-predictable basaltic volcanism from a lithospheric mantle source (central Basin and Range Province, USA), *Earth Planet. Sci. Lett.*, 261, 201–216, doi:10.1016/j.epsl.2007.06.029.

Valentine, G. A., and F. V. Perry (2009), Volcanic risk assessment at Yucca Mountain, Nevada, USA: Integration of geophysics, geology, and modeling, in *Volcanism, Tectonism, and Siting Nuclear Facilities*, edited by C. Connor, L. Connor, and N. Chapman, Cambridge Univ. Press, in press.

Valentine, G. A., D. Krier, F. V. Perry, and G. Heiken (2005), Scoria cone construction mechanisms, Lathrop Wells volcano, southern Nevada, USA, *Geology*, 33, 629–632, doi:10.1130/G21459.1.

Valentine, G. A., F. V. Perry, D. Krier, G. N. Keating, R. E. Kelley, and A. H. Coghill (2006), Small-volume basaltic volcanoes: Eruptive pro-

ducts and processes, and posteruptive geomorphic evolution in Crater Flat (Pleistocene), southern Nevada, *Geol. Soc. Am. Bull.*, *118*, 1313–1330, doi:10.1130/B25956.1.

Valentine, G. A., D. J. Krier, F. V. Perry, and G. Heiken (2007), Eruptive and geomorphic processes at the Lathrop Wells scoria cone volcano, *J. Volcanol. Geotherm. Res.*, *161*, 57–80, doi:10.1016/j.jvolgeores.2006.11.003.

Vaniman, D. T., B. M. Crowe, and E. S. Gladney (1982), Petrology and geochemistry of hawaiite lavas from Crater Flat, Nevada, *Contrib. Mineral. Petrol.*, *80*, 341–357, doi:10.1007/BF00378007.

Viollet, P. L., O. Simonin, J. Olive, and J. P. Minier (1992), Modeling turbulent two-phase flows in industrial equipments, in *Computational Methods in Applied Sciences*, edited by C. Hirsch, J. Périaux, and E. Oñate, pp. 213–224, Elsevier Sci., New York.

Wahl, R. R., D. A. Sawyer, S. A. Minor, M. D. Carr, J. C. Cole, W. C. Swadley, R. J. Laczniak, R. G. Warren, K. S. Green, and C. M. Engle (1997), Digital geologic map database of the Nevada Test Site area, Nevada, *U.S. Geol. Surv. Open File Rep.*, *1978*, 97–140.

Woods, A. W., S. Sparks, O. Bokhove, A. LeJeune, C. B. Connor, and B. E. Hill (2002), Modeling magma-drift interaction at the proposed high-level radioactive waste repository at Yucca Mountain, Nevada, USA, *Geophys. Res. Lett.*, *29*(13), 1641, doi:10.1029/2002GL014665.

───────────────

S. Dartevelle, Earth and Environmental Sciences Division, Los Alamos National Laboratory, MS D443, Los Alamos, NM 87545, USA. (sdart@lanl.gov)

G. A. Valentine, Department of Geology, 777 Natural Sciences Complex, State University of New York at Buffalo, Buffalo, NY 14260-1350, USA. (gav4@buffalo.edu)